ADVANCED ENERGY MATERIALS
www.advenergymat.de

# Impact of Trap Depth on the Steady-State and Transient Photoluminescence in Halide Perovskite Films

*Jürgen Hüpkes, Uwe Rau, and Thomas Kirchartz**

**Within the field of halide perovskites, trap-assisted recombination is often considered to be synonymous with first-order recombination, that is, recombination that scales linearly with the charge-carrier concentration. However, the standard Shockley-Read-Hall statistics naturally predict that trap-assisted recombination can have any scaling between linear and quadratic with carrier density, depending on the position of the trap or defect that enables recombination. In an intrinsic semiconductor, the shallower a trap is, the more the recombination rate will scale quadratically with carrier density, and the more it will resemble radiative recombination in its behavior in any transient experiment. Here, the theoretical implications of the trap depth in general and shallow traps in particular on transient and steady-state experiments applied to halide perovskite samples for photovoltaic or optoelectronic applications are discussed.**

## 1. Introduction

The working principle of photovoltaics relies on the collection of photogenerated charge carriers at the electrodes. The process competing with charge extraction is charge recombination, which typically proceeds predominantly via nonradiative pathways. In most thin-film solar cell materials, the common understanding is that it is nonradiative recombination via localized states combined with the emission of multiple phonons[1–6] that is responsible for the majority of the recombination events in a working solar cell.[7,8] Thus, it is crucial to understand and characterize recombination via localized states in any material considered for use as a photovoltaic absorber material.

In the currently quite popular field of halide-perovskite photovoltaics, recombination is frequently studied with the toolbox of photoluminescence-based methods.[9–12] Here, both steady-state photoluminescence (PL)[13–17] transient PL[18–21] and even continuous transitions between these two extremes[19] are highly popular methods. All PL-based methods use the photons emitted by radiative recombination as the observable with the target of quantifying non-radiative recombination. Radiative recombination is unavoidable in highly absorptive semiconductors due to detailed balance.[22–26] Nonradiative recombination, however, is avoidable and could be suppressed by modifying processes of film preparation,[27–29] by modifying the chemical properties of interfaces,[30–35] the energy-level alignment at interfaces[36–39] or even the dielectric properties of the different layers.[40,41]

In halide perovskites, non-radiative recombination is typically much less severe than in many other materials that are or have been under investigation for possible use in photovoltaics[7,42,43] which has led to the frequently used description of halide perovskites as being defect-tolerant.[44,45] A common explanation for the high electronic quality of (at least) lead-halide perovskites is the shallow nature of most intrinsic point defects.[46–48] In the context of explaining and understanding photoluminescence experiments, it is nevertheless common practice to ignore the trap depth in the discussion and consider solely deep defects as well as radiative recombination.[19,49] We have recently shown[50–52] that this is a poor approximation in many situations, where especially the photoluminescence transients start to behave in a way that is inconsistent with frequently-used simplified versions of Shockley-Read-Hall (SRH) statistics.[53,54]

Here, we explore the implications of the energetic position of localized states on the performance of perovskite solar cells and on the steady-state and transient photoluminescence data. We start with a short discussion of the role of localized states in non-radiative multiphonon recombination, followed by a summary of the experimental evidence for shallow traps dominating recombination in relevant lead-halide perovskite compositions. Subsequently, we introduce the theoretical description of transient and steady-state photoluminescence in such a way that trap depth is explicitly included. Our aim is to provide a description of

J. Hüpkes, U. Rau, T. Kirchartz
IMD-3 Photovoltaics
Forschungszentrum Jülich
52425 Jülich, Germany
E-mail: t.kirchartz@fz-juelich.de
U. Rau
Jülich Aachen Research Alliance
JARA-Energy
and Faculty of Electrical Engineering and Information Technology
RWTH Aachen University
Schinkelstr. 2, 52062 Aachen, Germany
T. Kirchartz
Faculty of Engineering and CENIDE
University of Duisburg-Essen
Carl-Benz-Str. 199, 47057 Duisburg, Germany

The ORCID identification number(s) for the author(s) of this article can be found under https://doi.org/10.1002/aenm.202503157



**DOI: 10.1002/aenm.202503157**

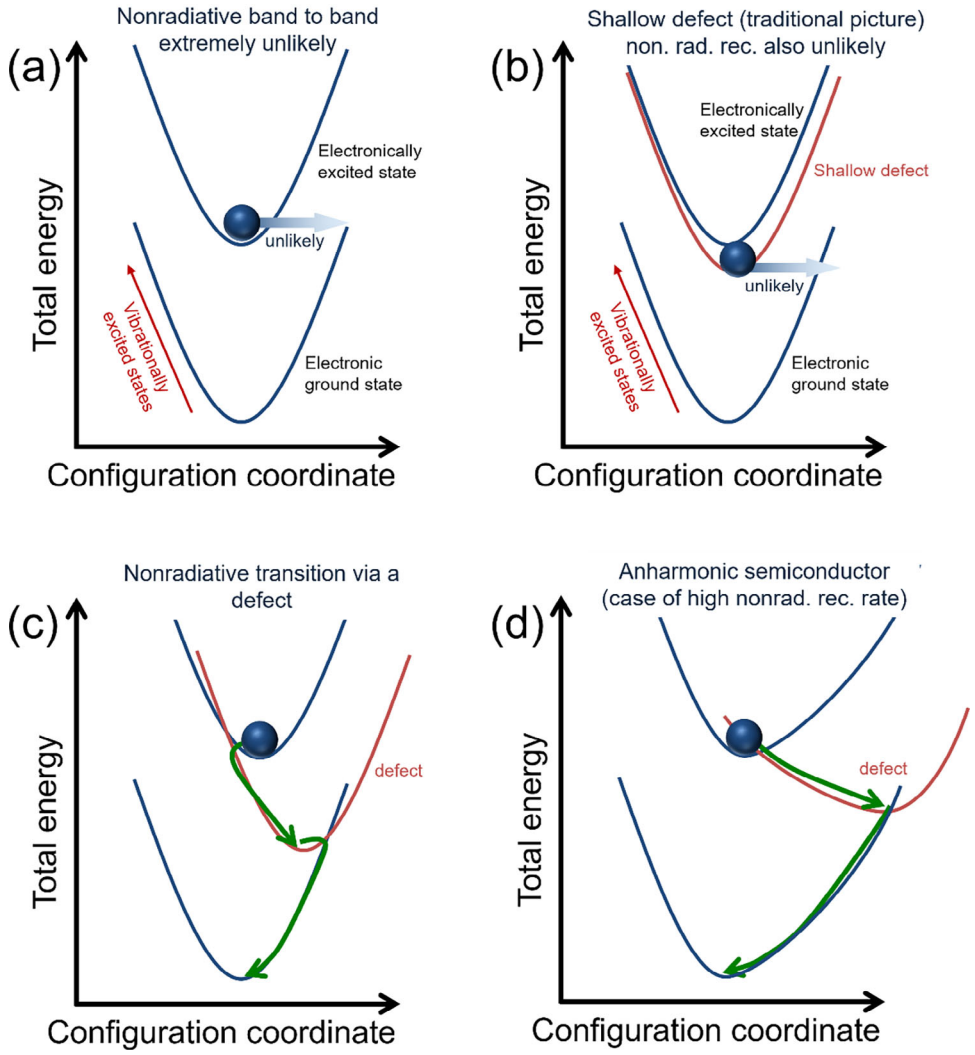


**Figure 1.** Schematic configuration coordinate diagrams to illustrate different situations for non-radiative recombination. a) Nonradiative band-to-band recombination in inorganic semiconductors is extremely unlikely due to the need to tunnel isoenergetically from the electronically excited state into a vibrationally excited state of the electronic ground state.[56] If the parabolas are only vertically offset (no reorganization energy of the defect-free crystal), this is nearly impossible. b) For a shallow defect, similar arguments would suggest that the transition to the ground state (in this case) is similarly unlikely. c) If the defect is deeper, the parabola is expected to be more significantly shifted on the x-axis (change the geometry of the crystal more), consequently leading to a higher likelihood for both transitions from the electronically excited state via the defect to the ground state. d) In case the semiconductor is anharmonic (the potential energy surfaces are not parabolic anymore), shallow defects may also end up leading to fast recombination. However, the anharmonicity may also cause the opposite, i.e., make a given transition less likely.

the underlying theory of recombination and photoluminescence that allows readers with different backgrounds to understand the implications of shallow defects. Thus, we provide sufficient background for the article to represent a stand-alone tutorial on recombination statistics and their implications for transient and steady-state photoluminescence in intrinsic semiconductors.

## 2. Analytical Descriptions of Photoluminescence

### 2.1. Localized States and Their Role in Recombination

Localized states that are often referred to either as traps or defects occur in the bulk of semiconductors but in higher concentrations at grain boundaries and interfaces. These states accelerate recombination as they increase the likelihood of multiphonon transitions.[55,56] In most inorganic semiconductors, band-to-band nonradiative transitions are extremely unlikely because of the negligible wave-function overlap of the electronically excited state relative to the vibrationally excited electronic ground state of the system (see **Figure 1a**). This wavefunction overlap only increases when states that are absent in the perfect periodic crystal are introduced into the system. In the presence of such structural defects, localized states are formed that force the crystal around them into a slightly different geometry. This change in geometry is the same concept that is referred to as the reorganization energy in molecular semiconductors.[57,58] However, this change of geometry may be small, as shown in Figure 1b, in which case the transition probability to the ground state would

not significantly increase relative to the case of the band-to-band transition shown in Figure 1a. Alternatively, it could be more significant as shown in Figure 1c. Now, nonradiative transitions via the localized state formed by the defect become possible and start to reduce the luminescence intensity, open-circuit voltage,[59,60] and eventually the efficiency of any photovoltaic device. Within the harmonic oscillator approximation, shallow defects have a low likelihood of interacting with the band that is further away from the defect (see Figure 1b).[61] They may trap and detrap one type of carrier, but they rarely dominate recombination. Therefore, the common understanding in the field has partly been that shallow defects exist, but that they do not play an important role in non-radiative recombination. It was rather the few deep defects that were thought to dominate recombination.

Lead-halide perovskites, however, are highly anharmonic semiconductors.[62,63] This implies that the potential-energy surfaces calculated from density functional theory calculations of specific defects differ particularly strongly from the parabolic shapes[5,6,61,64] predicted by the harmonic oscillator model (see Figure 1c vs d for schematic examples and **Figure 2** for three concrete examples).[1] The implication of this finding is that the attempt to infer a likely magnitude of the capture coefficients purely from the energetic position of a given defect is unlikely to be accurate.[6] Consequently, we cannot a priori rule out that there are shallow defects in lead-halide perovskites that also interact efficiently with the band that is energetically further away. Furthermore, there is evidence from first-principles calculations (see Figure 2 and **Table 1**) that there exist specific defects in metal-halide perovskites that are rather shallow and interact better with the band that is energetically further away. One example is the H-vacancy created by removing H from an N atom existing, e.g., in methylammonium. Here, the resulting defect is close to the valence band but effectively interacts with the conduction band (see Figure 2c or ref. [1]). Also, other examples have been reported, such as those discussed in refs. [65] Furthermore, in more generic descriptions of multiphonon recombination, such as discussed, e.g., in refs. [5,66–68], a shallow trap would be expected to be only slightly shifted on the x-axis of the configuration coordinate diagram (see Figure 1b). However, in first principles calculations of actual defects (see Figure 2b or ref. [1]), the shift might be very significant as schematically illustrated in Figure 1d. The resulting possibility that shallow defects may indeed be the dominant path for recombination has important consequences for the way recombination is quantitatively and qualitatively analyzed[50,52] and it provides explanations for several observations in the literature that are difficult to explain otherwise. These observations include the power law decays that we will discuss in more detail in the following, but also the observation of non-radiative bimolecular recombination.[69,70]

An additional question to consider regarding localized states is their charge state. The two simplest scenarios are acceptor-like and donor-like defects. An acceptor-like defect is either negatively charged or neutral (−/0). Thus, if an acceptor-like defect is close to the valence band, it will act as a p-type dopant, meaning that already in thermodynamic equilibrium (no applied voltage, no illumination, no temperature gradients), the defect will be ionized (i.e., negatively charged), thereby creating a hole in the valence band as a counter charge. A donor-like defect is either positively charged or neutral (0/+), implying that if it is situated close to the conduction band, it will be empty and therefore act as an n-type dopant. It creates a free electron whose countercharge is a positively charged defect. In addition, the so-called amphoteric defects may have more than two charge states, that is, positive, neutral, and negative. In this article, we restrict ourselves to singly charged defects and focus on acceptor-like defects for the sake of simplicity. Table 1 provides a summary of DFT calculations of defect states using the Heyd-Scuseria-Ernzerhof

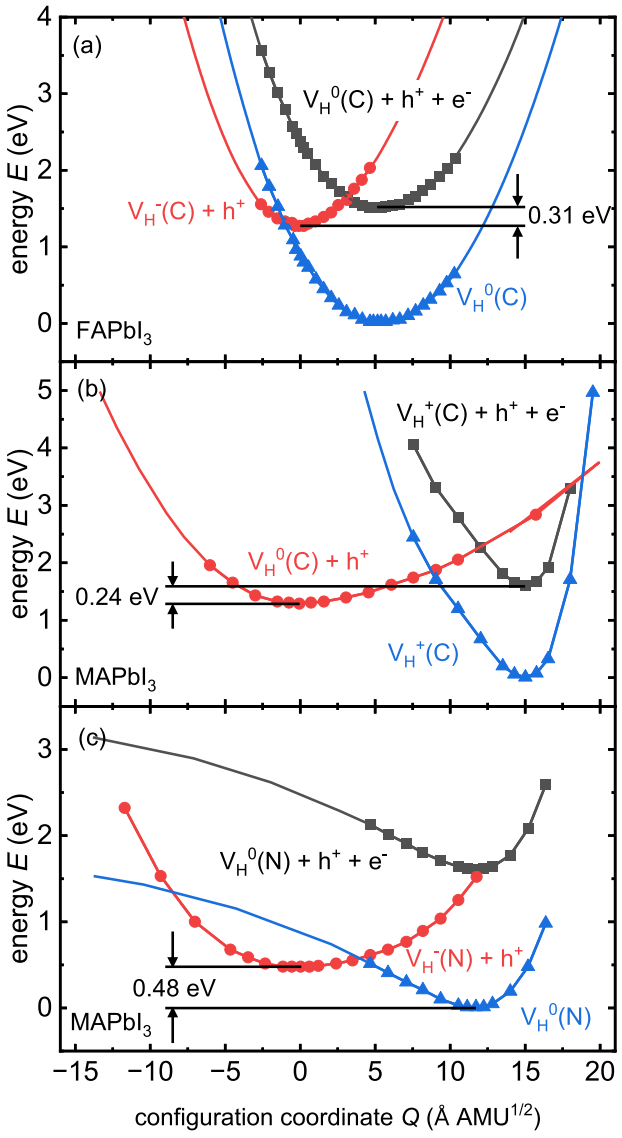


**Figure 2.** Configuration coordinate diagrams calculated for different hydrogen vacancies in perovskites: a) $V_H$(N) depicts a hydrogen vacancy created by removing hydrogen from a nitrogen atom in $FAPbI_3$. This represents a rare example of an acceptor-like defect close to the conduction band. b) Configuration coordinate diagram of a hydrogen vacancy at the C-atom in $MAPbI_3$. This is an example of a donor-like defect close to the conduction band that should, in principle, dope the perovskite already in the dark without applied bias. c) Configuration coordinate diagram of a hydrogen vacancy at the N atom in $MAPbI_3$. This is an example of an acceptor-like defect below midgap that would be partly ionized in the equilibrium (i.e., dope the perovskite p-type but not very efficiently).

**Table 1.** Calculated defect levels in different perovskite materials from the literature. Defect energies significantly lower than mid-gap are marked in bold. Defects that contribute to doping (acceptor-like defects close to the valence band or donor-like defects close to the conduction band) show the acceptor/donor column in bold and shallow traps, which only cause photo-doping, have their defect type bold printed.

| Material | Defect | Acceptor/Donor | Trap energy | | Bandgap [eV] | Capture coefficients | | Refs. |
|---|---|---|---|---|---|---|---|---|
| | | | $E_C$–$E_T$ [eV] | $E_T$–$E_V$ [eV] | | $\beta_n$ [cm$^3$ s$^{-1}$] | $\beta_p$ [cm$^3$ s$^{-1}$] | |
| $MAPbI_3$ | $I_I$ (+/0) | D | 0.49 | 1.01 | 1.50 | | | [71] |
| $MAPbI_3$ | $I_I$ (+/0) | D | 0.51 | 1.08 | 1.60 | $7 \times 10^{-9}$ | | [72] |
| $MAPbI_3$ | $I_I$ (+/0) | D | 0.57 | 1.01 | 1.59 | | | [73] |
| $MAPbI_3$ | $I_I$ (+/0) | D | 0.64 | 0.94 | 1.58 | | | [74] |
| $MAPbI_3$ | $I_I$ (0/−) | A | 0.84 | 0.74 | 1.60 | | $4 \times 10^{-8}$ | [72] |
| $MAPbI_3$ | $I_I$ (0/−) | A | 1.28 | 0.30 | 1.59 | | | [73] |
| $MAPbI_3$ | $I_I$ (0/−) | A | 1.35 | 0.15 | 1.50 | | | [71] |
| $MAPbI_3$ | $I_I$ (0/−) | A | 1.45 | 0.13 | 1.58 | | | [74] |
| $MAPbI_3$ | $I_{MA}$ (−/2−) | A | 0.59 | 0.91 | 1.50 | | | [71] |
| $MAPbI_3$ | $I_{MA}$ (0/−) | A | 1.33 | 0.16 | 1.50 | | | [71] |
| $MAPbI_3$ | $I_{MA}$ (+/0) | D | 0.00 | 1.58 | 1.59 | | | [73] |
| $MAPbI_3$ | $I_{Pb}$ (+/0) | D | 0.04 | 1.55 | 1.59 | | | [73] |
| $MAPbI_3$ | $V_H$(C) (+(0) | D | 0.31 | 1.29 | 1.59 | $8 \times 10^{-18}$ | $3 \times 10^{-16}$ | [1] |
| $MAPbI_3$ | $V_H$(N) (0/−) | A | 1.12 | 0.48 | 1.59 | $1 \times 10^{-4}$ | $2 \times 10^{-4}$ | [1] |
| $MAPbI_3$ | $V_I$ (+/0) | D | 0.00 | 1.58 | 1.59 | | | [73] |
| $MAPbI_3$ | $V_I$ (+/0) | D | 0.08 | 1.50 | 1.58 | | | [74] |
| $MAPbI_3$ | $V_I$ (0/−) | A | 0.01 | 1.48 | 1.50 | | | [71] |
| $MAPbI_3$ | $V_{Pb}$ (−/2−) | A | 1.44 | 0.15 | 1.59 | | | [73] |
| $MAPbI_3$ | $V_{Pb}$ (−/2−) | A | 1.51 | 0.07 | 1.58 | | | [74] |
| $MAPbI_3$ | $V_{Pb}$ (0/−) | A | 0.75 | 0.84 | 1.59 | | | [73] |
| $MAPbI_3$ | $V_{Pb}$ (0/−) | A | 1.24 | 0.34 | 1.58 | | | [74] |
| $MAPbBr_3$ | **$I_{Br}$ (+/0)** | D | 1.53 | **0.73** | 2.26 | | | [75] |
| $MAPbBr_3$ | $I_{Br}$ (0/−) | **A** | 2.14 | **0.13** | 2.26 | | | [75] |
| $MAPbBr_3$ | $I_{MA}$ (+/0) | **D** | **0.05** | 2.21 | 2.26 | | | [75] |
| $MAPbBr_3$ | $I_{Pb}$ (+/0) | **D** | **0.79** | 1.47 | 2.26 | | | [75] |
| $MAPbBr_3$ | $V_{Br}$ (+/0) | **D** | **0.03** | 2.24 | 2.26 | | | [75] |
| $MAPbBr_3$ | $V_{Pb}$ (−/2−) | **A** | 2.11 | **0.16** | 2.26 | | | [75] |
| $MAPbBr_3$ | $V_{Pb}$ (0/−) | **A** | 1.63 | **0.64** | 2.26 | | | [75] |
| $FAPbI_3$ | **$V_H$(C) (0/−)** | A | **0.24** | 1.28 | 1.50 | $3 \times 10^{-8}$ | $3 \times 10^{-5}$ | [1] |
| $CsSnI_3$ | $V_I$ (+/0) | **D** | 0.06 | 1.24 | 1.29 | $3 \times 10^{-14}$ | $9 \times 10^{-8}$ | [76] |
| $CsSnI_3$ | **$V_I$ (0/−)** | A | 0.51 | 0.83 | 1.27 | $2 \times 10^{-6}$ | $1 \times 10^{-14}$ | [76] |
| $CsGeI_3$ | $V_I$ (+/0) | **D** | 0.46 | 1.14 | 1.60 | $5 \times 10^{-8}$ | $4 \times 10^{-19}$ | [76] |
| $CsGeI_3$ | **$V_I$ (0/−)** | A | 0.52 | 1.08 | 1.58 | $3 \times 10^{-30}$ | $2 \times 10^{-29}$ | [76] |

(HSE)[77] functional with spin orbit coupling, where we state the type of defect (including charge state), energetic position relative to either band, as well as the capture coefficients at room temperature (where available). For the use of an HSE functional with spin-orbit coupling relative to earlier approaches, see, e.g., refs. [71,74]. We highlighted the respective lower energetic distance of the defects to either of the two bands. The bold letters in the "Acceptor/Donor" column indicate moderate or significant ionization of the defect state in equilibrium, leading to doping.

**Figure 3** illustrates the different scenarios that can occur regarding the charge states of shallow defects. The upper row illustrates acceptor-like defects, and the lower row shows donor-like defects. The first column shows the scenario in which the defects are primarily neutral, that is, empty in the case of the acceptor-like trap and occupied with electrons in the case of the donor-like traps. In this case, the defect density does not lead to significant shifts in the equilibrium Fermi level, and the semiconductor behaves intrinsically in the dark. One potential representative of such a defect in $MAPbI_3$ is the iodine vacancy, which may create an acceptor-like defect very close to the conduction band.[71] The second column illustrates the scenario where the defects do cause a shift in the equilibrium Fermi level. Panel (e) shows how the trap energy of an acceptor-like trap affects the equilibrium density of holes for different trap densities. If the acceptor-like trap is close to the conduction band (situated at 1.6 eV above the valence band edge), the equilibrium hole density will be extremely low. However, if the trap is close to the valence band, the equilibrium hole density approaches the trap density. Thus, the equilibrium

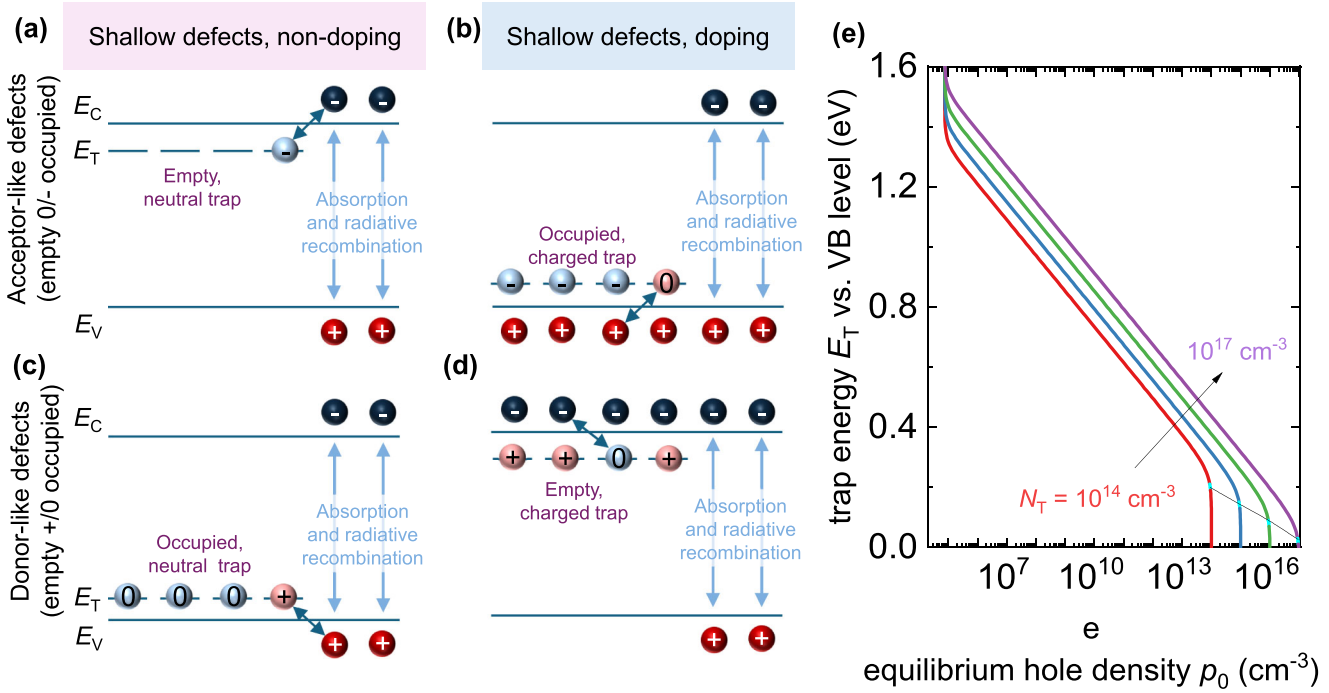


**Figure 3.** a–d): Schematic of a band diagram of a semiconductor with charge carriers generated from optical absorption and from capture of charge carriers in shallow defects. The diagrams represent acceptor-like defects close to the conduction band a) and valence band (b), and donor-like defects close to the conduction band (c) and valence band (d). The panels (a) and (c) represent shallow defects that do not contribute to the charge carrier density in equilibrium but act as traps or recombination centers, while in (b) and (d), the traps contribute to the equilibrium charge-carrier density as dopants. Panel (e) shows the equilibrium hole density $p_0$ for traps with a certain density $N_T$ at a certain energetic position $E_T$ relative to the valence band.

hole concentration can vary by many orders of magnitude for the same defect density.

### 2.2. Literature Observations Compatible with Shallow Traps

The main purpose of this paper is to discuss the implications of a combination of low doping densities[78] and shallow defects on the recombination statistics of semiconductors in general and halide perovskites in particular. To motivate this approach, we will discuss the experimental evidence that supports the approach in the following section. **Figure 4a** shows transient PL data that follows a power-law type decay of the photoluminescence after approximately hundreds of nanoseconds, reaching up to the hundred microsecond mark in one of the datasets.[50] In semiconductor physics, it is customary to quantify the speed of recombination via a quantity called the charge carrier lifetime. The logic of the charge carrier lifetime becomes particularly obvious in situations where recombination is linear in charge carrier density. Then, the excess carrier density $\Delta n$ will decay exponentially with time and a characteristic time constant $\tau$ can be determined from such a decay. Thus, if $\Delta n(t) = \Delta n(t) \exp(-t/\tau)$, an exponential fit will provide the time constant $\tau$ which will

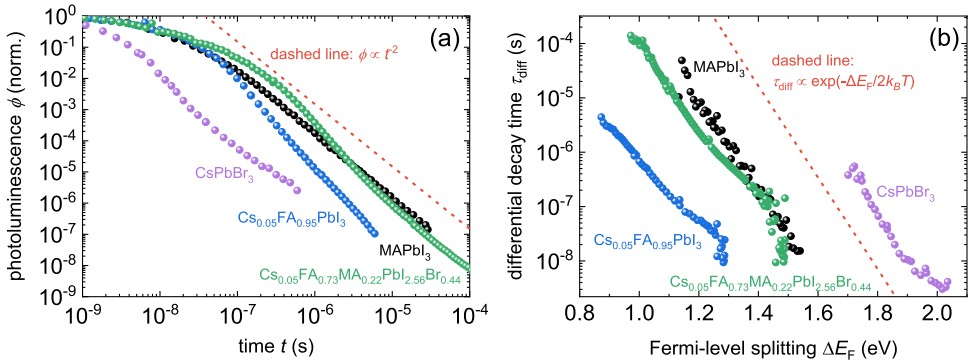


**Figure 4.** a) Normalized PL decays of perovskite films on a double-logarithmic scale. The reference line $\phi_{TPL} \propto t^{-2}$ is plotted for comparison. b) Differential decay time $\tau_{diff}$ versus Fermi-level splitting $\Delta E_F$ corresponding to the decays shown in (a). The reference line $\tau_{diff} \propto \exp(-\Delta E_F/(2k_BT))$ is shown for comparison. Figure reproduced from ref. [50] under the terms of the CC-BY 4.0 license. © The authors of ref. [50].

contain all information on the speed of the decay and the material properties responsible for the decay. However, even in reasonably well-behaved semiconductors such as crystalline silicon, the approach of just fitting one exponential to any transient data was insufficiently complex as usually several recombination mechanisms were superimposed.[79,80] Typically, the time constant $\tau$ would depend on the carrier density and thereby on the excitation conditions (e.g., laser power of the pulsed laser used for excitation) and in transient experiments also on the time after the excitation. Thus, rather than using a single or even multiple exponential fits to a decay curve, it became more common in the silicon world to determine the logarithmic derivative of the decay as a function of the excess carrier density.[81] A similar approach is also useful in the context of halide perovskite films. Figure 4b shows the associated differential decay times resulting from the data shown in Figure 4a. The differential decay time is determined from the photoluminescence flux $\phi_{\mathrm{TPL}}$ via[18]

$$\tau_{\mathrm{diff}} = \left(-\frac{1}{2}\frac{d\ln(\phi_{\mathrm{TPL}})}{dt}\right)^{-1} \tag{1}$$

where $t$ is the time after the laser pulse. The factor 2 considers the fact that the luminescence flux $\phi_{\mathrm{TPL}} \propto np$, which simplifies to $\phi_{\mathrm{TPL}} \propto n^2$ in materials with low doping concentrations such as halide perovskites. Thus, if we consider the defining equation for the decay time to be

$$\tau_{\mathrm{diff}} := \left(-\frac{d\ln(n)}{dt}\right)^{-1} = -\frac{n(t)}{dn(t)/dt} \tag{2}$$

then the equation to determine $\tau_{\mathrm{diff}}$ from experimental data, must include a factor 2 as seen in Equation (1). Equation (2) is designed such that if we apply it to a simple exponential decay of the type $\Delta n(t) = \Delta n(t)\exp(-t/\tau)$, we would obtain $\tau_{\mathrm{diff}} = \tau$, i.e., a constant decay time.

However, given that the decays in Figure 4a are power laws rather than exponentials, the application of Equation (1) to the data leads to continuously changing decay times. To understand how they are changing with injection condition (i.e., with carrier density $n$ or Fermi level splitting $\Delta E_{\mathrm{F}}$), it is most instructive to start with a differential equation that eventually produces a power-law as seen in Figure 4a. This is the case for a differential equation of the type

$$\frac{dn}{dt} = -kn^2, \tag{3}$$

where $k$ is a recombination coefficient of unit $\mathrm{cm}^3/\mathrm{s}$. The exact physical mechanism represented by $k$ is not important for the moment. It could be radiative recombination or, as we will later see, recombination via sufficiently shallow defects. Currently, we are only interested in the signatures of such a quadratic differential equation in the experimental data. Equation (3) can now be solved either for $n(t)$ or directly for $\tau_{\mathrm{diff}}$ using the right-hand side of Equation (2). The former approach yields

$$n(t) = \frac{n(0)}{1 + kn(0)t}, \tag{4}$$

which is for long times a power-law relation between $n(t)$ and time $t$, where $n(0)$ is the carrier density directly after the laser pulse. If $\phi_{\mathrm{TPL}} \propto n^2$ holds, Equation (4) implies that for longer times ($t > (kn(0))^{-1}$), $\phi_{\mathrm{TPL}} \propto t^{-2}$ will result, which is indicated by the red dashed line in Figure 4a. The latter approach to directly solve Equation (3) for $\tau_{\mathrm{diff}}$ directly yields

$$\tau_{\mathrm{diff}} = \frac{1}{kn} \tag{5}$$

which—in the limit of high-level injection ($n = p$)—leads to $\tau_{\mathrm{diff}} \propto \exp(-\Delta E_{\mathrm{F}}/(2k_{\mathrm{B}}T))$ which is indicated with a red dashed line in Figure 4b. Thus, we note that the observation of power-law decays for long times and high laser fluences (high values of $n(0)$) directly results in a decay time that scales exponentially with Fermi-level splitting. An additional observation, discussed in detail in Ref. [50], can be obtained by inserting Equation (4) into Equation (5) to express the differential decay time as a function of time rather than the carrier density or Fermi-level splitting. The result is ref. [50]

$$\tau_{\mathrm{diff}} = \frac{1}{kn(0)} + t \tag{6}$$

which implies that for long times ($t > (kn(0))^{-1}$) or high fluences, the decay time $\tau_{\mathrm{diff}} \approx t$. This result means that plotting a decay time as a function of time for a decay that is power law in nature does not result in any information other than that it is indeed a power law decay. All information on the material, which is encoded in the recombination coefficient $k$, is lost. Thus, in this paper, we will directly show the decay time as a function of Fermi-level splitting to avoid this information loss.

The observation of power-law decays, as shown in Figure 4, is not often reported in literature as most data are not plotted on double-logarithmic scales and do not have sufficient signal-to-noise ratio and dynamic range to observe the difference between, for instance, a bi-exponential decay and a power-law decay. Furthermore, the "1" in the denominator of Equation (4) is a crucial term in understanding the PL decay in systems that approximately obey Equation (3). Only once the "1" is negligible relative to $kn(0)t$, the decay really follows a power law (i.e., a straight line in Figure 4a). For situations where the opposite is true, the decay will be difficult to distinguish in its shape from the beginning of an exponential decay. The reason is that the Taylor expansion up to the first-order term of Equation (4) gives

$$n(t) = \frac{n(0)}{1 + kn(0)t} \approx n(0)\left(1 - kn(0)t\right) \tag{7}$$

This result is notably functionally the same as that for any exponential decay ($\exp(-x) \approx 1 - x$ for small values of $x$). Thus, whether any given decay is rather exponential or power law in its nature requires a certain dynamic range and time interval to distinguish. Especially in those situations, where the decay is still approximately linear in time, the solutions of $dn/dt = -kn^2$ and $dn/dt = -n/\tau$ would not differ at all in their functional dependence on time.

Figure 4 shows decays that were measured using a gated CCD camera for photon detection. Thanks to its internal amplification, it is straightforward to measure with a sufficient dynamic

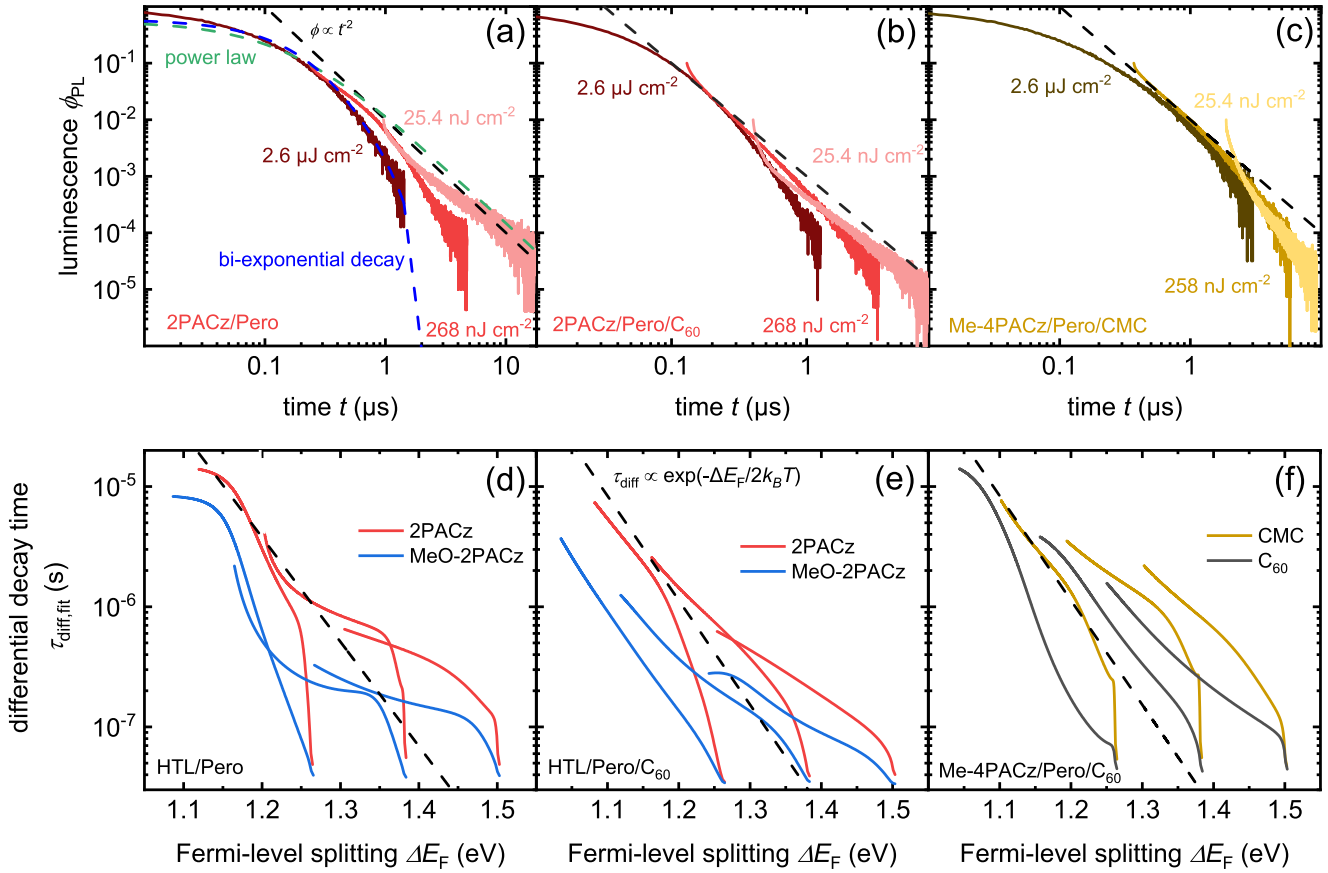


**Figure 5.** a–c) Transient PL measurements on different perovskite layer stacks, including a hole transport layer in each case and an electron transport layer in the case of panel (c). Each of the samples is based on a glass/ITO substrate that additionally contains the layers, as denoted in the lower left corner of each figure. d–f) Differential decay time versus quasi-Fermi-level splitting for three laser intensities and different samples that always include the one shown in the upper row and one additional sample not shown there. Figure reproduced from ref. [82] under the terms of the CC-BY 4.0 license. © The authors of ref. [82].

range to observe the condition $t > (kn(0))^{-1}$ that facilitates identifying a decay originating from a differential equation of the type $dn/dt = -kn^2$. The most frequently used type of photon detection for transient PL measurements is, however, the time-correlated single-photon counting technique. This technique does not easily enable dynamic ranges of larger than four orders of magnitude in luminescence. However, it is relatively simple to measure several times with different initial laser fluences and combine the resulting data.

In **Figure 5**a we have added a guide-to-the-eye line for the power law decay, which is well followed by the experimental data for long times. In addition, we show fits to these curves based on a bi-exponential decay and a power law, which includes the constant mentioned in Equation (7). The frequently used biexponential decay may describe the experimental decay under certain restrictions of short lifetimes of deep traps, but we clearly demonstrate that the biexponential curve drops more rapidly and cannot describe the decay for long times in this case. This fact is often overlooked in the literature, because many experimental data are available with limited dynamic range only (see Figure 1b in ref. [52]). Futhermore, data in the literature is frequently studied on semilogarithmic plots with a linear time axis, where deviations from multiexponential fits are more difficult to identify than in the rarely used double-exponential depictions of the data.

Figure 5 illustrates the impact of laser fluences on the appearance of (a-c) PL decays and (d-f) differential decay times of the different layer stacks.[82] All samples were deposited on a glass/ITO substrate and additionally contained a hole transport layer (HTL) and, in the case of the last column of figures, an electron transport layer (ETL). In the first row (a–c), the PL decays are shown such that the measurements performed at lower fluences (indicated by the labels 1OD and 2OD) are offset in luminescence intensity by one order of magnitude (1OD) and two orders of magnitude (2OD) and offset in time such that they fit best to the data from the higher fluence. This shows that these multilayer structures also exhibit non-exponential decays that roughly follow a power law at longer times. The second row of panels (d–f) shows the resulting differential decay times. These show in parts a double S-shape (panel d) and in parts a rather straight line after an initial steep region at higher values of $\Delta E_F$. The steeper region at high $\Delta E_F$, i.e., earlier times, corresponds primarily to an initial decay of the PL due to either trapping or diffusion of charge carriers. The region at lower $\Delta E_F$ and later times corresponds to the region dominated by recombination. The different fluences always show a fairly consistent behavior at later times,

while the decay times at early times change rapidly to approach the common trend at later times. None of the datasets shows a classical exponential decay, as one would expect from a deep trap. Thus, the essence of Figures 4 and 5 is that the normal situation in many lead halide perovskite absorber layers and layer stacks is non-exponential recombination with decay times that exhibit a carrier-density-dependent trend over a significant part of the observed range. Such non-exponential decays or continuously changing decay times have also been reported using different experimental methods such as photo-Hall measurements,[83] quasi-steady-state photoconductivity decay,[84] and transient microwave conductivity.[85,86]

The question now is which physical mechanisms are consistent with the observed behavior. In the following, we will show that the data are consistent with recombination via defect states, where the defects are quite close to one of the band edges but not at all close to midgap. This can lead to a behavior that can be approximately described by Equation (3). Thus, we will now delve into the impact of the energetic positions of traps or defects on the typical observables in steady-state and transient photoluminescence.

## 3. Analytical Descriptions of Photoluminescence

### 3.1. Steady-State Photoluminescence

Throughout the article, we will continuously compare steady-state with transient photoluminescence and choose a way to represent the results of the calculations that we will explain in the following. For steady-state PL, we chose the external luminescence quantum efficiency as a figure of merit. The luminescence quantum efficiency is defined as

$$Q_e^{lum} = \frac{q\phi_{em}}{J_{rec}} \tag{8}$$

where $\phi_{em}$ is the emitted photon flux in units of $1/(cm^2 s)$, $q$ is the elementary charge, and $J_{rec}$ is the recombination current density. The luminescence quantum efficiency is defined such that higher values always imply less nonradiative recombination, which is nearly always beneficial for any photovoltaic device. Only in the specific case of exciton splitting in organic, molecular semiconductors, lower luminescence-quantum efficiencies may indicate better exciton splitting, which is good for photovoltaic functionality. However, in the context of lead-halide perovskites considered for photovoltaic applications, exciton splitting is normally of no concern as free carriers are created at room temperature.

For the case of a film on glass, where parasitic absorption can be assumed negligible, we can rewrite Equation (8) to represent rates instead of fluxes and arrive at

$$Q_e^{lum} = \frac{k_{rad}\left(1-p_r\right)np}{R_{SRH} + k_{rad}\left(1-p_r\right)np + R_{Aug}} \tag{9}$$

Here, $k_{rad}$ is the radiative recombination coefficient, $p_r$ is the reabsorption probability,[87] $R_{SRH}$ is the SRH recombination rate, and $R_{Aug}$ is the Auger recombination rate. To simplify the equation, it is possible to replace $k_{rad}(1- p_r)$ with an external radiative recombination coefficient $k_{e,rad} = k_{rad}(1- p_r)$, which is already corrected for the effect of reabsorption and photon recycling.[88,89]

Our aim is to understand the effect of the energetic position of the trap within the bandgap on the figures of merit, such as the luminescence quantum efficiency. Within the logic of Equation (9), the energy position of the trap enters via the SRH recombination rate, which can be written in steady state as Ref. [53]

$$R_{SRH} = \frac{np - n_0p_0}{\left(n+n_1\right)\tau_p + \left(p+p_1\right)\tau_n} \tag{10}$$

where $n_1 = N_C \exp(-\frac{E_C-E_T}{k_B T})$, $p_1 = N_V \exp(\frac{E_V-E_T}{k_B T})$, $\tau_n = (\beta_n N_T)^{-1}$, $\tau_p = (\beta_p N_T)^{-1}$ $n_0$, and $p_0$ are the equilibrium electron and hole concentrations, $\beta_n$ and $\beta_p$ are the capture coefficients of electrons and holes, $E_C$ is the conduction band edge, $E_V$ is the valence band edge, $E_T$ is the trap position in energy, $N_C$ is the effective density of states in the conduction band, $N_V$ the effective density of states in the valence band, and $N_T$ is the trap density. The trap position, the main topic of this article, is encoded in Equation (10) in the values of $n_1$ and $p_1$, a nomenclature going back to the original article by Shockley and Read.[53] These should not be mistaken for actual concentrations of charge carriers that physically exist somewhere in the semiconductor. Instead, $n_1$ and $p_1$ are abbreviations of unit carrier density that appear in the SRH equation if written in the form seen in Equation (10) and that consider the detrapping of charge carriers from a trap to the closest band. They can be understood as the hypothetical concentrations of free electrons and holes, assuming that the Fermi level is at the trap level. As understanding Equation (10) primarily requires one to distinguish between cases, where the Fermi level is above or below the trap level, these situations can be conveniently expressed by inequalities of the type $n \ll n_1$ meaning that the Fermi level is below the trap level and $n \gg n_1$ meaning that the Fermi level is above the trap level.

As $n_1p_1 = n_0p_0$, only one of the two quantities ($n_1$ or $p_1$) can be of comparable magnitude to $n$ and $p$ during the operation of a solar cell (where $np \gg n_0p_0$). Therefore, for the remainder of the article, we may assume that the trap is either midgap or above midgap, which would imply that we must only consider $n_1$ but not $p_1$. Furthermore, as lead-halide perovskite layers typically have extremely low doping densities,[78] there will be situations where it is sensible to simplify Equation (10) using the approximation $n = p$. In this scenario, we can simplify Equation (10) to

$$R_{SRH} \approx \frac{n^2}{\left(n+n_1\right)\tau_p + n\tau_n} \tag{11}$$

We can now also write an equation for the external luminescence quantum efficiency that relates parameters such as the lifetimes $\tau_n$ and $\tau_p$ as well as the trap depth $E_T$ directly to $Q_e^{lum}$. Neglecting Auger for simplicity, we arrive at

$$Q_e^{lum} = \frac{k_{e,rad}n\left(\tau_n + \tau_p + \tau_p\frac{n_1}{n}\right)}{1 + k_{e,rad}n\left(\tau_n + \tau_p + \tau_p\frac{n_1}{n}\right)} \tag{12}$$

Thus, at high values of $n$, where the 1 in the denominator is negligible, $Q_e^{lum}$ approaches unity. For sufficiently low values of

$n$, however, the luminescence quantum efficiency will saturate to a value $Q_e^{lum} = k_{e,rad} n_1 \tau_p / [1 + k_{e,rad} n_1 \tau_p]$ determined by the trap depth.

### 3.2. Transient Photoluminescence

The figure of merit, which we primarily study in the context of transient PL, is the differential decay time. We define the differential decay time via (see also Equation 1)

$$\tau_{diff} = \left( -\frac{1}{2} \frac{d \ln(\phi_{TPL})}{dt} \right)^{-1} \tag{13}$$

that is, via a logarithmic derivative of the PL flux with respect to time. To better understand the implications of the definition given by Equation (13), let us briefly discuss a simple case. For a deep defect and again neglecting Auger recombination, the differential equation determining the electron concentration in an intrinsic semiconductor ($n = p$) is given by

$$\frac{dn}{dt} = -R(n) = -k_{e,rad} n^2 - \frac{n}{\tau_n + \tau_p} \tag{14}$$

Furthermore, we know that $\phi_{TPL} \propto n^2$. Hence, $\tau_{diff} = (-\frac{1}{2} \frac{d \ln(\phi_{TPL})}{dt})^{-1} = -\frac{n}{dn/dt}$ and we therefore find[90,91]

$$\tau_{diff} = -\frac{n}{dn/dt} = \frac{1}{k_{e,rad} n + 1/(\tau_n + \tau_p)} \tag{15}$$

Thus, for high values of $n$, we obtain $\tau_{diff} = (k_{e,rad} n)^{-1}$, while for low values of $n$, we find $\tau_{diff} = \tau_n + \tau_p$. Thus, the definition given by Equation (13) is designed such that it provides the sum of the two SRH lifetimes as the output for the differential decay time if the SRH recombination dominates. The factor 2 in Equation (13) takes care of the fact that perovskites are intrinsic semiconductors and $\phi_{TPL} \propto n^2$. Thus, for methods such as transient-absorption spectroscopy or transient photoconductivity, where the observed signals are proportional to $n$, a similar definition as given by Equation (13), but without the factor 2, would lead to a consistent treatment. A key simplification in Equation (14) is that we describe the kinetics of charge carriers with one ordinary differential equation. In particular, we have not (yet) included an equation that considers the change in the density $n_T$ of the trapped electrons. We also do not consider diffusion, any form of detrapping, and assume that electrons can recombine, but they can never be re-emitted into the conduction band from a trap. All these assumptions are currently only applied for didactic reasons to provide an intuitive understanding of Equation (13).

There are now two levels of complexity in the description of (shallow) traps that we can add. The first level would still be entirely analytical and assumes that we have only a small density of shallow defects; thus, the charge trapped in these defects does not significantly change over time. Mathematically, this implies that $dn_T/dt << dn/dt$ and $n_T << n$. In this case, the key assumptions used to derive the steady-state Equations (10) and (11) are still given, and we can include the impact of detrapping by only considering $n_1$. The implication here is that detrapping does not significantly affect $n$ or $p$ but slows down recombination by increasing the numerator in Equation (11). Because detrapping is fast for a shallow acceptor-like trap close to the conduction band, the trap will be mostly empty. Thus, there are few electrons in the trap that can recombine with holes, thereby slowing down recombination. In this case, we arrive at a differential decay time given by

$$\tau_{diff} = \frac{\tau_n + \tau_p + \tau_p \frac{n_1}{n}}{1 + k_{e,rad} n \left( \tau_n + \tau_p + \tau_p \frac{n_1}{n} \right)} = \frac{Q_e^{lum}}{k_{e,rad} n} \tag{16}$$

As we used the steady-state solution of the SRH recombination rate to derive $\tau_{diff}$, it is obvious that the information contents of $\tau_{diff}$ and $Q_e^{lum}$ are basically identical. In a sample where the above-discussed approximations are valid, the only benefit of measuring both quantities would be to determine $k_{e,rad} n = Q_e^{lum} / \tau_{diff}$.

### 3.3. Results for Low Trap Densities

We will now illustrate the implications of the analytical equations derived so far for low densities of trap states and show their limitations. We will initially use the luminescence quantum efficiency $Q_e^{lum}$ as the quantity representing a steady state experiment and the differential decay time representing a transient experiment. Note that for the case of low trap densities, the information content is similar. Thus, **Figure 6** shows the calculated luminescence quantum efficiency $Q_e^{lum}$ and differential lifetime as a function of the quasi-Fermi level splitting $\Delta E_F$ for (a, b) deep defects with varying lifetime and (c,d) for a variation of the trap depth $E_T$. Here, the differential lifetime is calculated using the analytical formula (solid lines) after Equation (16). The dashed lines represent the calculated limit for long decay times, and the dotted lines represent the numerical calculations of the decay. The simulation parameters are found in **Table 2**.

Figures 6a and b are primarily an illustration of Equations (12) and (15). The luminescence quantum efficiency for a deep trap follows a simplified version of Equation (12), whereby the term with $n_1$ can be neglected. We therefore obtain $Q_e^{lum} = k_{e,rad} n(\tau_n + \tau_p) / [1 + k_{e,rad} n(\tau_n + \tau_p)]$ which approaches unity for high carrier densities $n$. For low values of $n$, the luminescence quantum efficiency just follows $Q_e^{lum} = k_{e,rad} n(\tau_n + \tau_p)$, i.e., it increases linearly with $n$. This is equivalent to saying that $k_B T \ln(Q_e^{lum}) \propto \Delta E_F + const.$, i.e., on a semilogarithmic plot of $Q_e^{lum}$ versus $\Delta E_F$, the increase will appear as a straight line as seen in Figure 6a. The longer the SRH lifetime $(\tau_n + \tau_p)$, the more the transition from the linearly increasing region to the region where $Q_e^{lum} \approx 1$ is shifted toward lower charge carrier densities or Fermi-level splittings $\Delta E_F$.

The differential decay time shown in Figure 6b follows the equation $\tau_{diff} = (k_{e,rad} n + 1/(\tau_n + \tau_p))^{-1}$ (see Equation 15). For high values of the carrier density $n$ and the Fermi-level splitting $\Delta E_F$, radiative recombination will dominate and $\tau_{diff} = (k_{e,rad} n)^{-1}$ will decrease with increasing $n$. For low values of the carrier density $n$ and the Fermi-level splitting $\Delta E_F$, SRH recombination will dominate, and the decay time will saturate to a constant value given by $\tau_{diff} = \tau_n + \tau_p$. For both Figures 6a,b, the trap is assumed

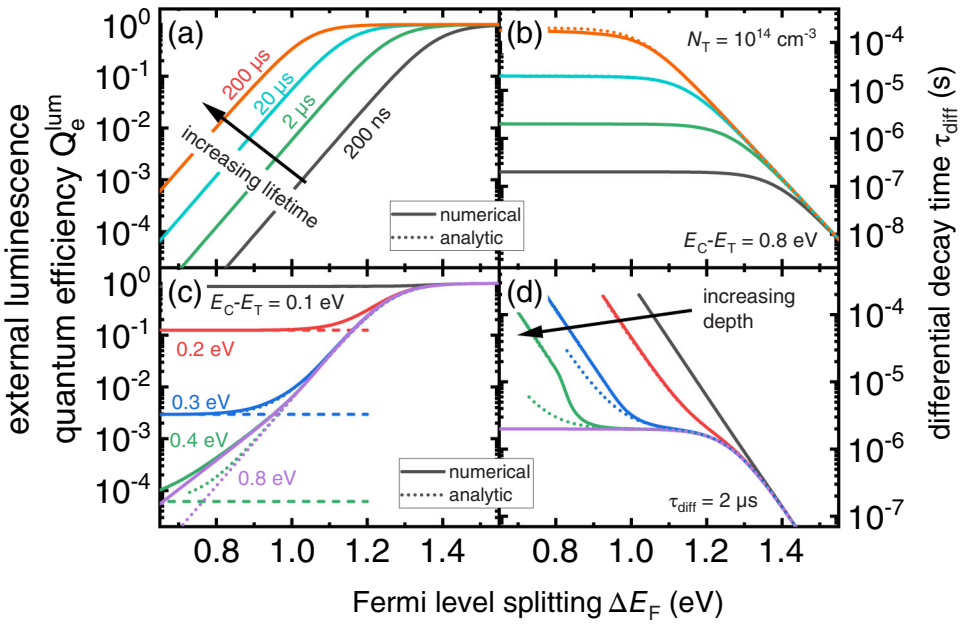


**Figure 6.** a,c) External luminescence quantum efficiency $Q_e^{lum}$ and b,d) differential decay time $\tau_{diff}$ as a function of the quasi-Fermi level splitting $\Delta E_F$ for the variation of (a,b) the lifetime of a symmetric, deep trap and (c,d) for the variation of the energetic distance of the trap to the conduction band $E_T$. The trap density was rather low at $N_T = 10^{14}$ cm$^{-3}$. Note that for diminishing trap densities, the numerical solutions approach the analytic solutions. Simulation parameters are presented in Table 2.

to be perfectly midgap (i.e., at 0.8 eV distance to both conduction and valence band, assuming a 1.6 eV bandgap). Thus, the trap position is so far of no relevance as long as the trap is deep. This means that it doesn't matter for these calculations whether the trap is at 0.8 or 0.85 eV from the valence band edge as long as it is inside the two Fermi levels for electrons and holes within the range of Fermi-level splittings shown. This can be rephrased in terms of carrier densities: The position of the trap does not matter as long as $n$ and $p$ are higher than $n_1$ and $p_1$ for all carrier densities shown in the figure.

Figure 6c,d change the position of the trap in such a way that these conditions are violated. We are moving the trap toward the conduction band such that $n_1$ becomes a relevant term in Equation (10). Instead of two regions (increasing and constant) for $Q_e^{lum}$ versus $\Delta E_F$, we now observe three regions (constant, increasing, and constant again). From low to high values of $\Delta E_F$, the regions can be understood from Equation (12) and are given by $Q_e^{lum} = k_{e,rad} n_1 \tau_p / [1 + k_{e,rad} n_1 \tau_p]$ for low $\Delta E_F$, then a transition region that follows the same trajectory ($Q_e^{lum} = k_{e,rad} n(\tau_n + \tau_p)$) independent of trap depth (i.e., independent of $n_1$), and finally the saturation at $Q_e^{lum} \approx 1$.

Correspondingly, also the differential decay time will show three regions: $\tau_{diff} = \frac{n_1}{n} \tau_p / [1 + k_{e,rad} n_1 \tau_p]$ at low $\Delta E_F$, followed by a constant decay time independent of trap depth ($\tau_{diff} = \tau_n + \tau_p$) and finally the radiative-recombination limited decay time given by $\tau_{diff} = (k_{e,rad} n)^{-1}$. Notably, the constant intermediate region always provides the same decay time, but the range in which this decay time is valid changes dramatically with trap depth. The shallower the trap, the smaller the intermediate region, where $\tau_{diff} = \tau_n + \tau_p$.

**Table 2.** Parameters used for the simulations: Trap energy $E_T$ relative to the valence band with trap density $N_T$, capture coefficients for electrons $\beta_n$ and holes $\beta_p$, pulse energy equivalent to an initial excess charge density $n(0)$. The following parameters were kept constant: $E_g$ = 1.6 eV, $N_C = N_V = 2.2 \times 10^{18}$ cm$^{-3}$, $k_{e,rad} = 1.5 \times 10^{-10}$ cm$^3$s$^{-1}$.

| Figure | $E_T$ [eV] | $N_T$ [cm$^{-3}$] | $\beta_n$ [cm$^3$s$^{-1}$] | $\beta_p$ [cm$^3$s$^{-1}$] | $\tau_{n,p}$ [µs] | $n(0)$ [cm$^{-3}$] | $n_1$ [cm$^{-3}$] | $p_1$ [cm$^{-3}$] | comment |
|---|---|---|---|---|---|---|---|---|---|
| 3(e) | var | var | – | – | – | 0 | | | |
| 6 (a,b) | 0.8 | $10^{14}$ | var | var | var | $10^{18}$ | 7500 | 7500 | deep |
| 6 (c,d) | var | $10^{14}$ | $1 \times 10^{-8}$ | $1 \times 10^{-8}$ | 1 | $10^{18}$ | | | Shallow, low density |
| 9 | var | $10^{18}$ | $2 \times 10^{-12}$ | $2 \times 10^{-12}$ | 1 | $10^{18}$ | | | Shallow, high density |
| 11 | var | $10^{18}$ | $2 \times 10^{-12}$ | $2 \times 10^{-12}$ | 1 | $10^{18}$ | | | Shallow, high density |
| 13 | 1.5 | $10^{18}$ | $2 \times 10^{-12}$ | $2 \times 10^{-12}$ | 1 | var | $4.6 \times 10^{16}$ | $1.2 \times 10^{-7}$ | Shallow, high density |

## 4. Charge Neutrality and Steady State Photoluminescence

### 4.1. Acceptor-Like Traps Above Midgap

Equation (12) for the luminescence quantum efficiency has been derived for the assumption $n = p$. While lead-halide perovskites show only low doping densities in the dark,[78,92] it is unlikely that shallow traps would contain exactly as much positive charge as they contain negative charge. Thus, we must consider the possibility that in semiconductors with sufficient densities of shallow traps, discrepancies between electron and hole densities show up under illumination. This phenomenon has been termed photodoping, and there is some evidence that it exists in halide perovskites.[49,93] The first treatment of photodoping in the context of halide perovskites is by Stranks et al.[20] who developed a model based on SRH statistics that included excitons and more notably also the charge neutrality condition. The inclusion of the latter was decisive the reproducing features observed in transient and steady-state experiments and led the authors to conclude that there could be a large density of trapped electrons whose charge would then be counterbalanced by an approximately equal density of free holes. The concept was used to explain observations such as the photoconductivity of halide perovskites.[94] An important further step was the observation by Feldmann et al.[49] that transient PL decays (signal ~ $np$) and transient absorption decays (signal ~ $n$+$p$) were showing a behavior that was, for all *mixed* halide samples, inconsistent with the assumption that $n = p$. Thus, given the intrinsic nature[78] of the lead-halide perovskites in the dark, this was also a strong indication of photodoping. This observation was subsequently explained via lateral bandgap inhomogeneities, e.g., originating from halide segregation, a phenomenon that is unique to mixed halide samples. This photodoping hypothesis, which was restricted in its applicability to stoichiometries that could show bandgap variations, was subsequently questioned by Das et al.[93] based on an estimate of the impact of the measured bandgap variations on the recombination rates. Furthermore, it is also counter to observations of power law PL decays over many orders of magnitude in mixed and mono-halide perovskites, as shown in Figure 4. While the power law behavior is no direct indication of photodoping, the attempt to model both steady-state and transient PL is discussed in ref. [52] indicates that photodoping is needed to quantitatively reproduce the data. Finally, novel spectroscopic methods such as the pulse-burst transient photoluminescence variant developed by Marunchenko et al.[95,96] shows that halide perovskites store significant densities of charge carriers, which implies that they most likely also store significant densities of charge (it would be unlikely that the trapped negative and trapped positive charges were exactly equal in density).

In the following, we will illustrate some of the consequences of photodoping on the PL quantum efficiency. One peculiar result of photodoping is that the luminescence quantum efficiency will actually increase with trap density (and therefore increasing effect of photodoping) if the SRH lifetimes are kept constant. To calculate what happens with photodoping, we have to consider the charge neutrality equation. This implies that we must make an assumption about the charge state of the trap. We could for instance, assume that the trap was acceptor-like, implying that its charge state is negative if occupied with an electron and neutral if empty. In this case, charge neutrality dictates that $n + n_T = p$. If the defect was donor-like, the possible charge states would be neutral if occupied and positive if empty. In this case, the condition is $n + n_T = p + N_T$. As we are considering traps above midgap for simplicity, donor-like traps would lead to some degree of $n$-type doping, while acceptor-like defects would not lead to a significant level of doping and are therefore more consistent with experimental observations.[78] Thus, our default condition for the remainder of the article will be acceptor-like defects above midgap.

In the case that $n$ and $p$ can differ from each other, the luminescence quantum efficiency in the presence of an acceptor like trap above midgap is given by

$$Q_e^{lum} = \frac{1}{1 + \frac{1}{k_{e,rad}\left(\left(n+n_1\right)\tau_p + p\tau_n\right)}} \tag{17}$$

We could now give $n$ as a variable, which would require us to work out the hole density $p$ from the charge neutrality condition. For this, we would have to calculate the density of trapped electrons from SRH statistics, which gives

$$n_T = \frac{n\tau_p N_t}{\left(\left(n + n_1\right)\tau_p + p\tau_n\right)} \tag{18}$$

for the present case. From Equations (17), (18) and the charge neutrality condition ($n + n_T = p$), we can eliminate $p$, determine $n$ as the (somewhat lengthy) solution of a quadratic equation, and reinsert the result into Equation (17) to calculate $Q_e^{lum}$. We provide the solution of this as a short MATLAB script to the interested reader. The result can be seen in **Figure 7**. Figure 7a shows the situation that has already been shown in Figure 6c and that represents a relatively low trap density $N_T = 10^{14}$ cm$^{-3}$, whereby the trap position $E_T$ is varied from 0.1 eV distance to the conduction band edge (black line) to 0.4 eV distance (green line). The capture coefficients for electrons and holes are equal and set by the condition that $\tau_p = \tau_n = (\beta_n N_T)^{-1} = 1$ µs. Figures 7b and 7c show the situations of increasingly high trap densities, whereby the SRH lifetimes are always kept at 1 µs, i.e., higher trap densities always mean lower capture coefficients such that their product stays constant. Despite the constant SRH lifetimes, the luminescence quantum efficiencies do change for a given trap depth. The higher the trap density, the higher the luminescence quantum efficiency will be for a given trap depth. This is due to higher asymmetries[40,41,97] between electron and hole densities that lead to lower non-radiative recombination rates at a given $np$ product and a given set of SRH lifetimes $\tau_p = \tau_n = 1$ µs. In this situation, the shallow traps are not improving the luminescence. They are the only factors that reduce the luminescence below 1. However, for the rather theoretical assumption of a given SRH lifetime of a shallow trap, it is better if there is a high density of shallow traps as opposed to a low density, as the photodoping effect of the shallow traps mitigates the detrimental effect of recombination via these same traps.

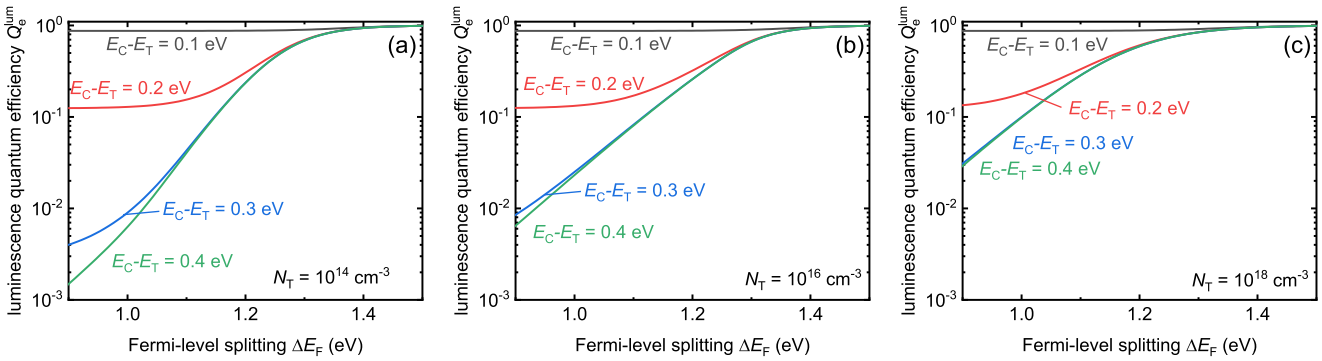


**Figure 7.** Effect of trap density and trap depth on the luminescence quantum efficiency assuming equal charge carrier lifetimes $\tau_n$ and $\tau_p$ (each 1 µs). Panels (a) to (c) show a continuously increasing trap density ranging from $N_T = 10^{14}$ cm$^{-3}$ in (a) to $N_T = 10^{18}$ cm$^{-3}$ in (c). Interestingly, an increase in trap density that coincides with a proportional decrease in capture coefficients ($\tau_p = \tau_n = (\beta_n N_T)^{-1} = 1$ µs) leads to higher luminescence quantum efficiencies once the shallow traps become charged and thereby lead to asymmetries in electron and hole densities (photodoping). The less shallow the trap, the bigger the effect, as the less shallow traps are more likely to be filled with electrons for a given Fermi-level splitting.

### 4.2. Acceptor-Like Traps Below Midgap

So far, we have discussed the impact of acceptor-like traps above midgap, i.e., traps that do not lead to significant doping in thermodynamic equilibrium, as the traps are above the Fermi-level and therefore empty and uncharged. Only under the application of forward bias or under illumination, the traps could fill to such a degree that their charge would start to matter. In the following, we also want to briefly cover the inverse situation of acceptor-like defects below midgap, which would be equivalent to studying donor-like defects above midgap. These two combinations represent situations where, depending on the exact depth of the trap, the traps are partly or even completely charged already in thermodynamic equilibrium. **Figure 8** presents the analogous simulation to Figure 7, where the traps are now below midgap and still acceptor-like. As the charge state of the traps only affects the equations via the charge-neutrality condition ($n + n_t = p$ for acceptor-like traps), Figure 8a looks identical to Figure 7a. Here, the distance to the next band affects the equations, but the charge state does not because of the low defect density ($N_T = 10^{14}$ cm$^{-3}$). The higher the trap density, the more the result diverges from the one seen in Figure 7. The strongest effect naturally occurs for the highest trap density shown in Figure 8c. If we compare Figures 7c and 8c for equal trap depth (measured to the nearest band edge), we note that in Figure 8c, the luminescence quantum efficiency reaches a plateau for low values of $\Delta E_F$ much quicker, i.e., the transition region between the plateau at high and low $\Delta E_F$ spans a smaller range in $\Delta E_F$. The value of $Q_e^{lum}$ at the plateau can be calculated analytically, which we will illustrate in the following to enable the reader to better understand the trends in Figure 8. In the case dominating in Figure 8c, the luminescence quantum efficiency can be written as

$$Q_e^{lum} = \frac{1}{1 + \frac{1}{k_{e,rad}\tau_n(p+p_1)}} \tag{19}$$

where we neglected both $n$ and $n_1$. Note that $n$ is negligible relative to $p$ because of the doping effect of the acceptor-like traps and $n_1$ is negligible relative to $p_1$ because the traps are below midgap. For low values of $\Delta E_F$, Equation (19) predicts a plateau as the only

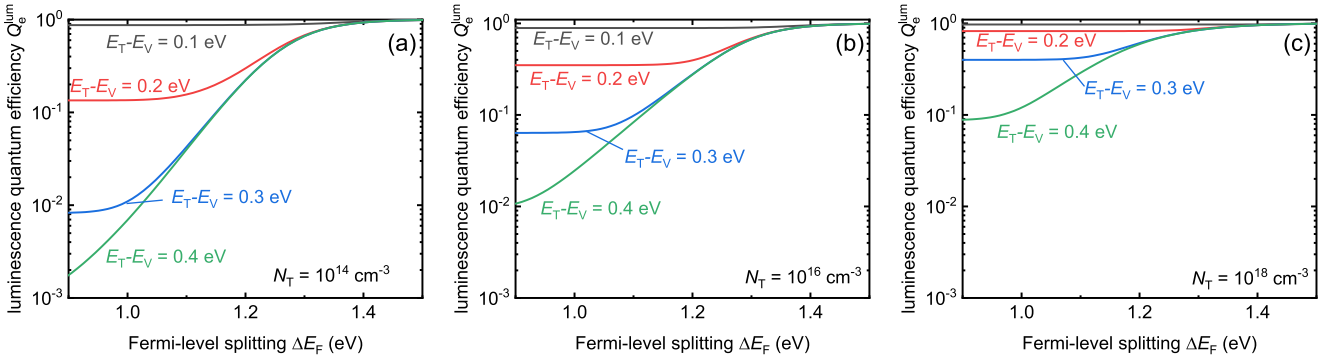


**Figure 8.** Same as Figure 7 but for the case of acceptor-like defects close to the valence band. Effect of trap density and trap depth on the luminescence quantum efficiency assuming equal charge carrier lifetimes $\tau_n$ and $\tau_p$ (each 1 µs). Panels (a) to (c) show a continuously increasing trap density ranging from $N_T = 10^{14}$ cm$^{-3}$ in (a) to $N_T = 10^{18}$ cm$^{-3}$ in (c). Panel (a) shows the same result as Figure 7a because for low densities, only the trap depth (to the nearest band) but not the density matters. Toward higher densities, the curves show a clearly visible plateau toward low values of $\Delta E_F$ that is given by the combination of Equations (19) and (21).

variable (namely $p$) also assumes a constant value at low $\Delta E_F$. This constant value is given by the condition

$$p = n_T = \frac{p_1 \tau_n}{\tau_n (p + p_1)} \tag{20}$$

where we assume again charge neutrality and that we can neglect $n$ and $n_1$. Equation (20) is a quadratic equation for $p$ that can be solved to give

$$p\,(n \ll p) = \frac{1}{2}\left(p_1 + \sqrt{p_1^2 + 4 p_1 N_t}\right) \tag{21}$$

Reinserting Equation (21) into Equation (19) provides an analytical solution for the constant low $\Delta E_F$ plateau of the luminescence quantum efficiency. This plateau primarily depends on $p_1$ and thereby on the trap depth and additionally on the trap density, which explains the shift of the plateau between Figure 8b,c. As higher values of $p$ increase $Q_e^{lum}$ if everything else stays constant, the increase in trap density (similar to an increase in doping density) increases $Q_e^{lum}$ as already observed in the context of Figure 7. This observation heavily rests on the assumption of both Figures 7 and 8 that the electron and hole lifetimes stay the same when the trap density changes.

## 5. Numerical Descriptions of Transient Photoluminescence

We have already noted in the discussion of Figure 6 that even for small trap densities, there is always a point on the $\Delta E_F$ axis, where the trap density is no longer small compared to the free electron and hole density. Thus, to theoretically describe the effect of shallow traps on *transient* experiments, we need to be able to also understand the more general situation, where the conditions $dn_T/dt \ll dn/dt$ and $n_T \ll n$ are not fulfilled. Now, we must leave the realm of analytical solutions and find a numerical solution to the time-dependent differential equations

$$\frac{dn}{dt} = -R_n = -R_{rad} - R_{nt} = -k_{e,rad} np - \beta_n n\left(N_T - n_T\right) + e_n n_T \tag{22}$$

for the electron density $n$,

$$\frac{dp}{dt} = -R_p = -R_{rad} - R_{pt} = -k_{e,rad} np - \beta_p p n_T + e_p\left(N_T - n_T\right) \tag{23}$$

for the hole density $p$, and

$$\frac{dn_T}{dt} = \beta_n n\left(N_T - n_T\right) - \beta_p p n_T - e_n n_T + e_p\left(N_T - n_T\right) = R_{nt} - R_{pt} \tag{24}$$

for the density $n_T$ of trapped electrons. Note that in Equations (22)–(24), we have used the rates $R_{nt}$, $R_{pt}$, and $R_{rad}$ for the exchange of electrons between the conduction band and the trap, for the exchange of holes with the traps, and for radiative recombination, respectively. The total rate for the electrons or holes read $R_n = R_{rad} + R_{nt}$ and $R_p = R_{rad} + R_{pt}$. With these definitions, we can rewrite Equation (13) as

$$\tau_{diff} = \left(-\frac{1}{2}\frac{d\ln(\phi_{TPL})}{dt}\right)^{-1} = \left(-\frac{1}{2}\frac{d\ln(k_{e,rad} np)}{dt}\right)^{-1}$$
$$= -2\left(\frac{1}{n}\frac{dn}{dt} + \frac{1}{p}\frac{dp}{dt}\right)^{-1} = 2\left(\frac{R_n}{n} + \frac{R_p}{p}\right)^{-1} \tag{25}$$

Owing to the detailed balance, the rates for the capture and emission of electrons and holes depend on each other. Therefore, Equations (22) to (24) can be rewritten, knowing that

$$e_n = \beta_n N_C \exp\left(\frac{E_T - E_C}{k_B T}\right) = \beta_n n_1 \tag{26}$$

and

$$e_p = \beta_p N_v \exp\left(\frac{E_v - E_t}{kT}\right) = \beta_p p_1 \tag{27}$$

Using Equations (22)–(27) in combination with charge neutrality, we can now simulate transient PL decays and the associated differential decay times as a function of carrier density or quasi-Fermi level splitting. However, it is also possible to derive approximate relations for situations not captured by Equation (16). These are situations where detrapping makes a significant contribution to the decay, which typically implies the presence of a high density of shallow traps. In the following, we study a situation in which an electron in a shallow trap (close to the conduction band edge) interacts faster with the electrons in the conduction band than with the holes in the valence band. Furthermore, we assume the trap to be close to the conduction band and hence mostly empty of electrons. In this case, the last two terms on the right-hand side of Equation (22) should be zero, i.e., $-\beta_n n N_T + \beta_n n_1 n_T = 0$ This condition is satisfied if $n = n_1 n_T / N_T$ Thus, the concentration of free electrons is proportional to the concentration of trapped electrons ($n \propto n_T$). If we look at Equation (24), we notice that the terms describing the interaction with the conduction band will be balanced out for ($-\beta_n n N_T + \beta_n n_1 n_T = 0$), while the term $e_p(N_T - n_T) \approx 0$. As we are in the situation, where $n \ll n_T$ and $n + n_T = p$ and $n + n_T = p$, the hole density and the density of trapped electrons must be identical ($n_T = p$) due to charge neutrality. Hence, we can also write $dn_T/dt = -n_T^2/(N_T \tau_p) - (k_{e,rad} n_1 p n_T)/N_T$. Thus, we already observe that we are dealing with a decay of trapped electrons that is quadratic in the trapped electron density. We now calculate the differential decay time via

$$\frac{1}{\tau_{diff}} = -\frac{1}{2}\frac{d\phi_{TPL}/dt}{\phi_{TPL}} = -\frac{1}{2}\frac{pdn/dt + ndp/dt}{np}$$
$$\approx -\frac{dn_T/dt}{n_T} = \frac{\left(1 + k_{e,rad}\tau_p n_1\right) n_T}{N_T \tau_p} \tag{28}$$

For convenience, it is possible to rewrite Equation (28) in terms of the free carrier densities or the quasi-Fermi level splitting by eliminating the density of trapped carriers via $n = n_1 n_T / N_T$ and $n_T = p$. We then arrive at

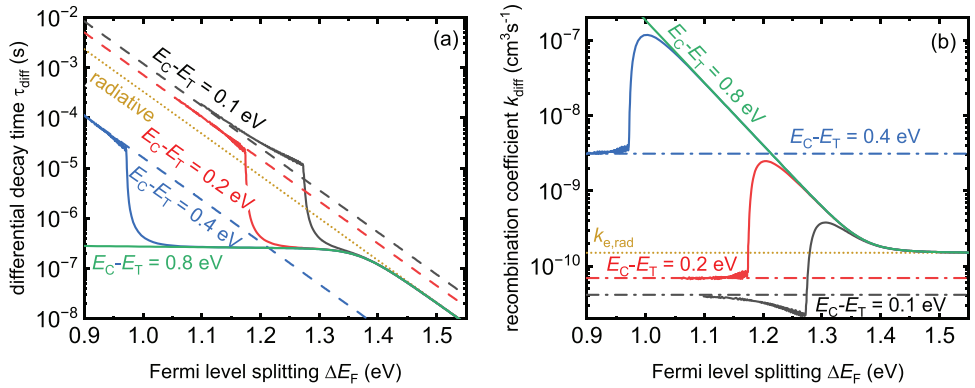


**Figure 9.** a) Differential decay time $\tau_{diff}$ and b) recombination coefficient $k$ as a function of the quasi-Fermi level splitting $\Delta E_F$ for high trap density $N_T = 10^{18}$ cm$^{-3}$ and the variation of the energetic trap position $E_T$ relative to the conduction band. Solid lines represent the transients based on numeric calculations; the dashed lines represent Equation (29), and the dash-dotted lines in (b) represent Equation (32). The dotted lines show the decay for simple radiative recombination.

$$\tau_{diff} \approx \tau_p \sqrt{\frac{n_1 N_T}{np}} \frac{1}{1 + k_{e,rad} \tau_p n_1}$$

$$= \tau_p \frac{\sqrt{n_1 N_T}}{n_i} \frac{1}{1 + k_{e,rad} \tau_p n_1} \exp\left(-\frac{\Delta E_F}{2 k_B T}\right) \quad (29)$$

where $n_i = \sqrt{n_0 p_0}$ is the intrinsic carrier density. Thus, we note that the differential decay time still scales exponentially with the Fermi level splitting in the same way as it does for a low concentration of shallow defects or for radiative recombination. However, the prefactors are different. While for low defect densities, the differential decay time approaches $\tau_{diff} = \tau_p \frac{n_1}{n} = \tau_p \frac{n_1}{\sqrt{np}}$ (see Equation (16)), for high defect densities the lifetime increases by a factor $\sqrt{n_1 N_T}/n_1 = \sqrt{N_T/n_1}$ if we neglect the terms with $k_{e,rad}$ for simplicity.

**Figure 9** shows the impact of the trap depth on transients for a high trap density $N_T = 10^{18}$ cm$^{-3}$. The transients are calculated numerically from rate equations (solid lines) and by using analytic formulas for low quasi-Fermi level splitting (a, dashed lines) after Equation (29). As predicted by Equation (29), the decay times are proportional to $\exp(-\Delta E_F/2k_B T)$, which leads to continuously changing decay times that only show an intermediate plateau. Thus, it is valid to question the use of a decay time as a sensible figure of merit for the data. A possible alternative figure of merit for recombination is known from research on semiconductors with primarily bimolecular recombination.[98–100] This is the case for organic semiconductors, where it is common to calculate an effective bimolecular recombination coefficient from transient or steady state data. The advantage is that in the presence of strong nonradiative recombination mechanisms that are quadratic in electron or hole density, an effective recombination coefficient is more likely to be constant with carrier density or Fermi-level splitting than a decay time. Thus, sample-to-sample comparisons become simpler.[98,101] In a steady-state situation, an effective recombination coefficient $k_{eff,cw}$ could be defined via

$$k_{eff,cw} = \frac{R_{cw}}{np} \quad (30)$$

where $R_{cw}$ is the total rate of recombination in a steady-state situation at an injection level given by a certain $np$-product. To come up with a definition for a transient experiment, we start with a simple differential equation of the form $dn/dt = -kn^2$ and recover $k$ from $n(t)$. Thus, a possible definition of the differential recombination coefficient extracted from a transient experiment would be $k_{diff} = -(dn/dt)/n^2$. However, in practice, we need a definition that (i) considers the fact that we have access to the luminescence (which is proportional to $np$) and (ii) is robust against the idea of photodoping that will lead to $n \neq p$. Thus, we propose the definition

$$k_{diff} = -\frac{1}{2\sqrt{np}} \frac{d \ln(\phi_{PL})}{dt} = -\frac{1}{2\sqrt{np}} \frac{d\phi_{PL}}{dt \phi_{PL}} \quad (31)$$

Here, we use only quantities that are either equal to or proportional to the luminescence flux $\phi_{PL}$. The geometric mean $\sqrt{np}$ of the free carrier densities can be inferred from the transient PL data in the following way. By measuring the laser power and considering the fraction of absorbed photons, it is possible to estimate the initial carrier concentration directly after the laser pulse has hit the sample. If we assume that recombination losses are negligible during the laser pulse and if we further use the information that lead-halide perovskites have a doping density that is orders of magnitude lower than carrier densities typically created by a laser pulse during a transient PL experiment, the initial value of $n = p = \sqrt{np}$ is known within the accuracy of the measurement of the laser power. Once recombination sets in and the luminescence decays as a function of time, we can use the fact that the luminescence is proportional to $np$, i.e., $\phi_{PL} \propto np$. Thus, every order of magnitude decay in $\phi_{PL}$, leads to a $\sqrt{10}$ decay in the geometric mean $\sqrt{np}$ of the carrier density. Thereby, the geometric mean of the carrier density can be determined at every point of the decay in the same way that the Fermi-level splitting can be determined. This statement holds true even if $n \neq p$ at times after the pulse due to asymmetric trapping of electrons and holes.

Using Equation (31), we can also determine an analytical approximation for the differential decay time for a high density of

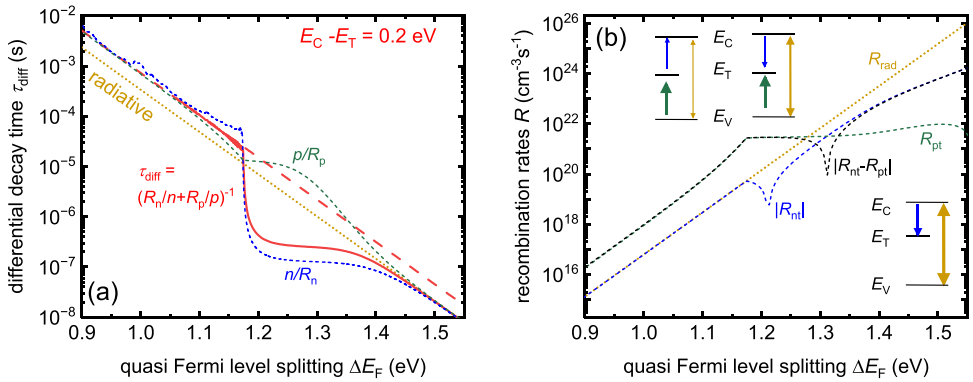


**Figure 10.** a) Differential decay time $\tau_{diff}$ for the trap energy $E_C - E_T = 0.2$ eV (from Figure 7a) and its decomposition into its electron and hole components $n/R_n$ and $n/R_n$. b) The rates $R_{nt}$, $R_{pt}$, and $R_{rad}$, as defined in Equations (22)–(24), change over many orders of magnitude as a function of the quasi-Fermi level splitting $\Delta E_F$ during the transient. The insets illustrate the dominant rates during the three phases: i) dominant radiative recombination combined with the filling of the trap by electrons at $\Delta E_F > 1.35$ eV. ii) The transition phase ($1.35 < \Delta E_F > 1.2$ eV) is defined by a reduced contribution of $R_{rad}$ and the fact that hole capture dominates over electron capture, i.e., $R_{pt} > R_{nt}$. Accordingly, the trap filling rate $R_{nt} - R_{pt}$ (black dashed line, displayed as absolute value) changes its sign from positive to negative. (iii) The final stage ($\Delta E_F < 1.2$ eV) is entirely determined by hole capture, and the capture of electrons turns into the emission of electrons, i.e., $R_{nt}$ (blue dashed line, displayed as absolute value) changes its sign from positive to negative.

shallow traps in the same logic as done for the differential decay time in Equation (29). This leads to

$$k_{diff} \approx \frac{1 + k_{e,rad}\tau_p n_1}{\tau_p \sqrt{n_1 N_T}} = \frac{1}{\tau_p \sqrt{n_1 N_T}} + k_{e,rad}\sqrt{\frac{n_1}{N_T}} \tag{32}$$

Notably, the analytical approximation given by Equation (32) gives a constant value independent of carrier density and Fermi-level splitting. Figure 9b illustrates the impact of applying Equation (31) to the same simulated PL decays as used for the decay times shown in Figure 9a. Now all parts of the decay time that had the slope $\tau_{diff} \propto \exp(-\Delta E_F/(2k_B T))$ in Figure 9a, now end up leading to $k_{diff} = \text{const}$ in Figure 9b. Thus, both at high and low Fermi-level splitting the numerical results for $k_{diff}$ become constant. For the higher Fermi level splittings the result is given by radiative recombination (dotted yellow line) and for lower Fermi level splittings, it is given by Equation (32) (dash-dotted line). In the intermediate region, a transition between the two levels is visible that produces some overshoot effects (i.e., it goes above the upper and below the lower of the two approximate results for high and low Fermi level splitting). This notably implies that $k_{diff}$ can be both larger but also smaller (!) than the radiative recombination coefficient $k_{e,rad}$. This is a phenomenon that is much unlike the steady state situation, where radiative recombination always marks the lower limit of the total recombination rate. This phenomenon is related to the effect of photodoping (i.e., $n \neq p$) and will be explained in the following.

To explain the fact that the measured differential lifetime is longer than the radiative lifetime, we must discuss how these lifetimes depend on the actual rates. Equation (25) describes that the differential lifetime $\tau_{diff}$ is composed of the inverse average of an electron contribution $n/R_n$ and a hole contribution $p/R_p$. Figure 10a shows how these two quantities develop as a function of the quasi-Fermi level splitting $\Delta E_F$ during one of the transients from Figure 8 ($E_C - E_T = 0.2$ eV) and how they influence the differential decay time $\tau_{diff}$. Notably, both components are almost equal in both regimes, where the decay time is proportional to $\exp(-\Delta E_F/2k_B T)$, namely for $\Delta E_F > 1.35$ eV and for $\Delta E_F < 1.2$ eV. In the first regime, we have $n \approx p$ and the decay time is defined by radiative recombination. Thus, we approximate Equation (25) by

$$\tau_{diff} = \frac{1}{2}\left(\frac{R_n}{n} + \frac{R_p}{p}\right)^{-1} \approx \frac{1}{2}\left(\frac{R_{rad}}{n} + \frac{R_{rad}}{p}\right)^{-1} = \frac{R_{rad}}{n} \tag{33}$$

The second regime is ($\Delta E_F < 1.2$ eV) is determined by the capture of holes into the trap while there is only a small number of free electrons. This latter fact causes some numerical noise for the electron contribution $n/R_n$ (blue dashed curve in **Figure 10a**) because its value is a quotient of very small numbers (albeit equal to the hole contribution $p/R_p$, which is the quotient of two much larger numbers).

Figure 10b shows the rates $R_{nt}$, $R_{pt}$, and $R_{rad}$ for electron capture, hole capture, and for radiative recombination as defined in Equations (22)–(24), as well as the difference $R_{nt} - R_{pt}$, which describes the filling of the trap with electrons (if $R_{nt} - R_{pt} > 0$) as well as it's emptying (if $R_{nt} - R_{pt} < 0$). In phase (i) ($\Delta E_F > 1.35$), the dominant rate is $R_{rad}$. Simultaneously, we observe the filling of the trap ($R_{nt} \gg R_{pt}$) by electrons. In the transition phase (ii) ($1.35 < \Delta E_F > 1.2$ eV), the contribution of $R_{rad}$ (yellow dotted line) is reduced and hole capture dominates over electron capture, i.e., $R_{pt} > R_{nt}$. Accordingly, the rate $R_{nt} - R_{pt}$ (black dashed line, displayed as absolute value) changes its sign from positive to negative. At the same time, the rate for hole capture (green dashed line) exceeds the radiative rate $R_{pt} > R_{rad}$, while the electron kinetics is still dominated by radiative recombination, i.e., $R_{nt} > R_{rad}$. In this regime, the differential decay time in Figure 10a is mostly determined by the electron contribution $n/R_n$. (iii) The final phase ($\Delta E_F < 1.2$ eV) is entirely determined by hole capture, simultaneously, the capture of electrons turns into the emission of electrons, i.e., $R_{nt}$ (blue dashed line, displayed as absolute value) changes its sign from positive to negative. The small number of electrons emitted from the trap recombines radiatively, leading to $-R_{nt} \approx R_{rad}$.

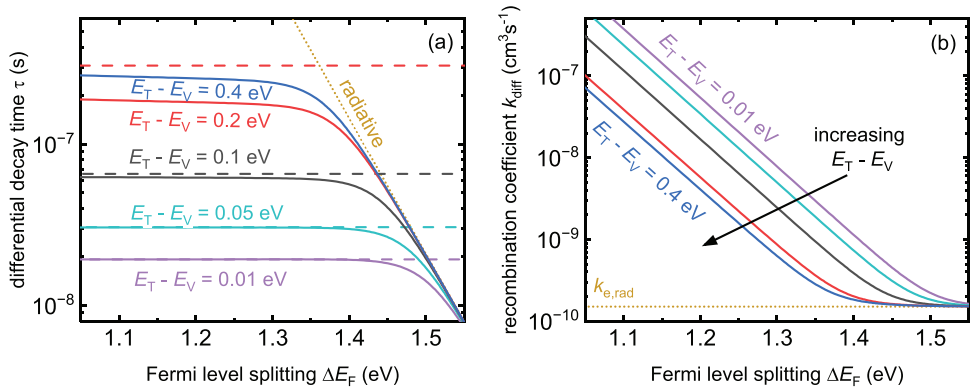


**Figure 11.** Analogous calculation to Figure 9, but for acceptor-like traps close to the valence band. a) Differential decay time $\tau_{diff}$ and b) recombination coefficient $k$ as a function of the quasi-Fermi level splitting $\Delta E_F$ for a high trap density $N_T = 10^{18}$ cm$^{-3}$ and the variation of the energetic trap position $E_T$ relative to the nearest band. Solid lines represent the transients based on numeric calculations. The dotted lines show the decay for simple radiative recombination. Dashed lines are derived from Equation (35). Simulation parameters can be found in Table 2.

In Figures 7 and 8, we highlighted the similarities and differences between simulations for acceptor-like defects above and below midgap. In the case of transient simulations, we do the same, whereby **Figure 11** presents the analogous graphical representation of acceptor-like defects below midgap to Figure 9, which was showing the above midgap case. The differential decay time shown in Figure 11a follows a behavior qualitatively similar to the one shown in Figure 6b. For high values of $\Delta E_F$, the decay time follows a trend, where $\tau_{diff} \propto \exp(-\Delta E_F/2k_B T)$ as expected for radiative recombination. This trend transitions into a constant decay time, i.e., an exponential decay toward lower values of $\Delta E_F$, whereby the trap depth defines the value of the decay time. The recombination coefficients shown in Figure 11b consequently show a constant value of $k_{diff} = k_{e,rad}$ for high $\Delta E_F$ whereas for low $\Delta E_F$, the recombination coefficient increases monotonously. The take-home message from these simulations is that shallow acceptor-like traps close to the valence band that hold a significant amount of charge already in the dark are unable to explain power-law decays over a wide range of $\Delta E_F$ values.

We derive an analytical equation for the lifetime plateau at low $\Delta E_F$ for this case. The acceptor-like state close to the valence band significantly contributes to p-type doping of the semiconductor. Thus, the equilibrium electron concentration is vanishing. The charge neutrality $p = n_T$ and the assumption of an equilibrium between trapping and detrapping of holes $\beta_p p n_T = \beta_p p_1 (N_T - n_T)$ leads to a quadratic equation that can easily be solved to

$$p_{eq} = -\frac{p_1}{2} + \sqrt{\frac{p_1^2}{4} + p_1 N_T} \tag{34}$$

With this constant hole density $p$, the second term of Equation (25) vanishes. When using Equation (22) under the assumption of very low emission rate for electrons $e_n n_T$ it simplifies further to

$$\tau_{diff} = -2\left(\frac{1}{n}\frac{dn}{dt}\right)^{-1} = \frac{2}{k_{e,rad} p_{eq} + \beta_n \left(N_T - p_{eq}\right)} \tag{35}$$

Interestingly, this equation also still holds for low trap densities.

Toward the end of this largely theoretical chapter on the PL decay in the presence of a high density of traps that leads to photodoping, we briefly return to experimental data found in the literature. For the data previously shown in Figure 4, we can also provide the differential recombination coefficients $k_{diff}$ to illustrate the applicability of Equation (31) to experimental data. All parts of the decay seen in Figure 4a that were perfectly proportional to $\phi_{PL} \sim t^{-2}$ will now end up being horizontal in Figure 12. This is the case in particular for the $MAPbI_3$ data as well as for the lower $\Delta E_F$ parts of the triple-cation and the $CsPbBr_3$ data. In contrast, the lower bandgap double cation perovskite ($CsFAPbI_3$) showed a decay that was power law but did not scale with $\phi_{PL} \sim t^{-2}$. Hence, for this sample (blue), $k_{diff}$ de-

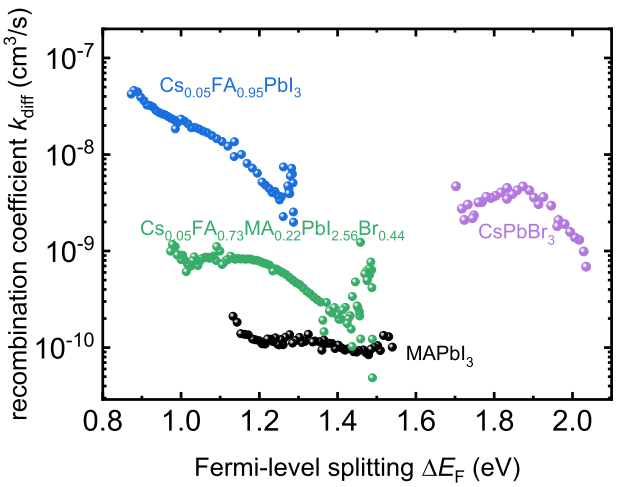


**Figure 12.** Recombination coefficient as a function of Fermi-level splitting for the PL transients shown in Figure 4a. Any parts of the original decay that are parallel to the dashed red line in Figure 4a that corresponds to the $\phi_{PL} \sim t^{-2}$ trajectory end up giving a constant value of $k_{diff}$. Any deviations from that trajectory lead to a dependence of $k_{diff}$ on carrier density or Fermi level splitting. Figure reproduced from ref. [50] under the terms of the CC-BY 4.0 license. © The authors of ref. [50].

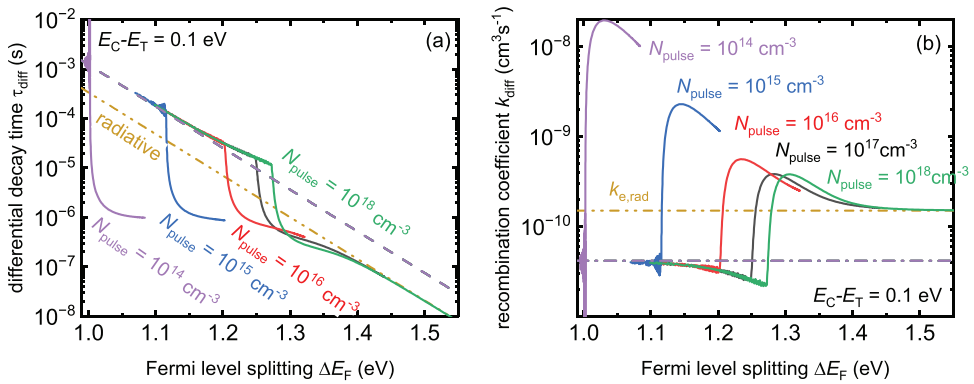


**Figure 13.** a) Differential decay time $\tau_{diff}$ and b) recombination coefficient $k_{diff}$ as a function of the quasi-Fermi level splitting $\Delta E_F$ for a shallow trap with varied fluence $N_{pulse}$ of the excitation. Solid lines represent the transients based on numerical calculations, the dashed lines represent Equation (29) and (32). The dash-dotted lines show the decay for simple radiative recombination. Simulation parameters can be found in Table 2.

viates significantly from the horizontal. However, compared to the differential decay time data shown in Figure 4b, the recombination coefficients are significantly more constant and therefore easier to compare. We note that the $MAPbI_3$ sample was made using a process leading to very luminescent films and solar cells with open-circuit voltages of ≈1.26 V for a bandgap of 1.6 eV.[18,102] Thus, it is plausible that this sample shows the lowest recombination coefficient. The triple-cation sample is discussed in more detail in ref. [52] was equally optimized for high luminescence and high open-circuit voltages in devices, and it is equally plausible that it has the second lowest recombination coefficients. The other two samples were not specifically optimized but used as references to show the generality of the effect.

## 6. Fluence Dependence

So far all simulations shown in the paper were performed assuming a high fluence such that the differential decay times or recombination coefficients would span as large a range in Fermi-level splittings as possible. It is a valid question to ask how a variation in pulse fluence, as we have seen it already in the experimental data shown in Figure 5 would affect the results. Figure 13 shows fluence-dependent simulations analyzed again in terms of (a) the differential decay time and (b) the recombination coefficient. The simulations are performed assuming a trap that is 0.1 eV below the conduction band edge, i.e., they correspond to the black line in Figure 9. Lower fluence implies that the initial carrier concentration at time $t = 0$ (immediately after the pulse) is lower. Thus, the decay times and recombination coefficient cover a range of Fermi level splittings that is shifted to the left of the figure and starts (on the right) at a lower maximum value of $\Delta E_F$. In addition, also the position of the jump from the yellow dash-dotted line to the purple dashed line (third phase in the discussion of Figure 9) shifts to lower values of $\Delta E_F$. However, it is noteworthy that all pulse fluences eventually approximate the dashed purple line that represents Equations (29) and (32).

## 7. Conclusions and Outlook

One of the central arguments why lead halide perovskites are particularly suitable for photovoltaic and optoelectronic applications is that intrinsic defects are primarily shallow.[47,103] While initial reports may have used unsuitable functionals for the DFT calculations[47,71], the general idea remained valid.[48] Nevertheless, the possible abundance of shallow defects was often considered as a sidenote by the spectroscopy and device physics communities that usually worked with deep defects to explain their data. The idea was that in most halide perovskites, a small density of deep defects may dominate the overall recombination rate despite a higher density of shallow defects and possibly mobile ions being present. Recombination via defects was considered to be generally linear in carrier density, leading to a high popularity of the so-called ABC model for explaining spectroscopic data.[19] However, going back to the full equations for recombination via defects in the SRH model[53,54] (or even the Sah-Shockley model[104] for amphoteric defects) immediately shows that recombination via defects can scale linearly or quadratic (or anything in between) with carrier density. The actual behavior of a given trap depends primarily on its energetic position in the bandgap (shallow versus deep), its density (does it contribute to the charge neutrality equation?), and its charge state (does it dope the sample in the dark, under illumination, or basically never?). While the theory for the statistics of recombination in semiconductors is already more than seven decades old, the application of that theory to the context of a near intrinsic semiconductor[78] with significant densities of shallow traps,[52] signs of photodoping[49] and power law decays[50] provides still interesting physical insights into how to analyze steady state and transient data sensitive to the recombination dynamics of the sample. Given the popularity of the technique, the current review focuses on photoluminescence-based techniques in steady state (PL quantum yield as a function of light intensity) and in the time domain. We proceed from situations of low to high complexity and discuss how the SRH model, in combination with the charge neutrality condition, results in different (approximate) results for the PL quantum yield and the PL decay. The central finding is that the presence of shallow traps can be deduced from the

dependence of the respective data on the carrier density or the Fermi-level splitting present for each recorded data point. Especially, in transient PL measurements, the observation of power-law decays that coincide with PL quantum yields significantly lower than 1 can easily be explained by recombination via shallow traps.

Future developments related to shallow traps and photodoping might involve strategies to directly access the electron and hole densities independently, which could be done, for instance, with photo-Hall measurements.[83,105] Furthermore, trapping and detrapping kinetics could be studied by adding additional degrees of freedom to the measurement. One approach previously discussed is the variation of fluence and repetition rate in the form of the so-called Horse plots[19,106] or alternatively the combination of very high and very low repetition rates in the form of pulse-burst measurements.[95,96] In case of the pulse burst measurements, the filling of traps results in a rise of the PL intensity during the burst phase (many pulses shortly after each other). After the burst phase is over, the PL slowly decays via recombination. As this measurement can also be done as a function of fluence and possibly temperature, it opens up more degrees of freedom than a traditional measurement with a fixed repetition rate would offer. Additional insights may also be accessible from systematic comparisons between different transient measurements that are sensitive to either the product or the sum of the electron and hole densities. One of the earliest papers that specifically talked about photodoping in halide perovskites was from Feldmann et al.[49] and used the combination of tr-PL and transient absorption spectroscopy as the key experimental insight to establish the existence of systematically different recombination dynamics between different samples. In the context of data analysis, the present paper focuses on analytical descriptions of PL and tr-PL that are useful to better understand the fundamental behavior of shallow versus deep traps. However, there may be situations where analytical equations are insufficiently complex to explain experimental observations. In this case, either numerical models must be fitted to the data[18] or the data analysis has to be done in the form of Bayesian parameter estimation[107–111] to quantify the likelihood of a certain set of parameters and a certain model to describe the data. Such approaches will help to quantify confidence in the result and will be able to help in quantifying the complementarity of different methods.

With respect to theoretical calculations of defect energy levels and recombination coefficients, we observe an interesting situation. Since the first publications from Yanfa Yan and coworkers,[46,47] many theoretical papers have highlighted the presence of shallow defects as an important feature of halide perovskites (see, e.g., the discussion in ref. [48] and references therein). However, the shallow defects that are featured in many theoretical studies are rather acceptor-like defects close to the valence band and donor-like defects close to the conduction band.[75,112] As these types of defects would lead to significantly different recombination kinetics than the one frequently observed (a power law in tr-PL over many orders of magnitude), it would be important to focus on the identification of point defects that could explain the observation of recombination kinetics consistent with shallow defects that are uncharged in thermodynamic equilibrium. An example of such a defect is shown in Figure 2a, but as this is a specific hydrogen vacancy in a formamidinium molecule, it is unlikely to be able to explain experimental observations discussed in this review that cover various compositions that do not include formamidinium.

## Acknowledgements

The authors acknowledge funding by the Helmholtz Association via the POF IV funding, via the project "Beschleunigter Transfer der nächsten Generation von Solarzellen in die Massenfertigung – Zukunftstechnologie Tandem-Solarzellen," via the Helmholtz.AI project AISPA – AI-driven instantaneous solar cell property analysis, as well as by the Deutsche Forschungsgemeinschaft (German Research Foundation) via the project "Correlating Defect Densities with Recombination Losses in Halide-Perovskite Solar Cells."

Open access funding enabled and organized by Projekt DEAL.

## Conflict of Interest

The authors declare no conflict of interest.

## Keywords

charge-carrier lifetime, decay time, photovoltaics, time-resolved photoluminescence

Received: June 10, 2025
Revised: August 20, 2025
Published online: September 18, 2025

[1] X. Zhang, J.-X. Shen, M. E. Turiansky, C. G. Van de Walle, *Nat. Mater.* **2021**, *20*, 971.
[2] A. Alkauskas, M. D. McCluskey, C. G. Van de Walle, *J. Appl. Phys.* **2016**, *119*, 181101.
[3] T. A. S. Doherty, A. J. Winchester, S. Macpherson, D. N. Johnstone, V. Pareek, E. M. Tennyson, S. Kosar, F. U. Kosasih, M. Anaya, M. Abdi-Jalebi, Z. Andaji-Garmaroudi, E. L. Wong, J. Madéo, Y.-H. Chiang, J.-S. Park, Y.-K. Jung, C. E. Petoukhoff, G. Divitini, M. K. L. Man, C. Ducati, A. Walsh, P. A. Midgley, K. M. Dani, S. D. Stranks, *Nature* **2020**, *580*, 360.
[4] J. S. Park, S. Kim, Z. Xie, A. Walsh, *Nat. Rev. Mater.* **2018**, *3*, 194.
[5] T. Kirchartz, T. Markvart, U. Rau, D. A. Egger, *J. Phys. Chem. Lett.* **2018**, *9*, 939.
[6] X. Zhang, M. E. Turiansky, J.-X. Shen, C. G. Van de Walle, *J. Appl. Phys.* **2022**, *131*, 090901.
[7] M. A. Green, A. W. Y. Ho-Baillie, *ACS Energy Lett.* **2019**, *4*, 1639.
[8] T. Kirchartz, U. Rau, *Adv. Energy Mater.* **2018**, *8*, 1703385.
[9] K. P. Goetz, A. D. Taylor, F. Paulus, Y. Vaynzof, *Adv. Funct. Mater.* **2020**, *30*, 1910004.
[10] T. Kirchartz, J. A. Márquez, M. Stolterfoht, T. Unold, *Adv. Energy Mater.* **2020**, *10*, 1904134.
[11] E. M. Hutter, T. Kirchartz, B. Ehrler, D. Cahen, E. v. Hauff, *Appl. Phys. Lett.* **2020**, *116*, 100501.
[12] M. B. Johnston, L. M. Herz, *Acc. Chem. Res.* **2016**, *49*, 146.
[13] M. Stolterfoht, M. Grischek, P. Caprioglio, C. M. Wolff, E. Gutierrez-Partida, F. Peña-Camargo, D. Rothhardt, S. Zhang, M. Raoufi, J. Wolansky, M. Abdi-Jalebi, S. D. Stranks, S. Albrecht, T. Kirchartz, D. Neher, *Adv. Mater.* **2020**, *32*, 2000080.
[14] M. Stolterfoht, P. Caprioglio, C. M. Wolff, J. A. Marquez, J. Nordmann, S. Zhang, D. Rothhardt, U. Hörmann, Y. Amir, A. Redinger, L. Kegelmann, F. Zu, S. Albrecht, N. Koch, T. Kirchartz, M. Saliba, T. Unold, D. Neher, *Energy Environ. Sci.* **2019**, *12*, 2778.

[15] V. Sarritzu, N. Sestu, D. Marongiu, X. Chang, S. Masi, A. Rizzo, S. Colella, F. Quochi, M. Saba, A. Mura, G. Bongiovanni, *Sci. Rep.* **2017**, *7*, 44629.
[16] D. Grabowski, Z. Liu, G. Schöpe, U. Rau, T. Kirchartz, *Sol. RRL* **2022**, *6*, 2200507.
[17] I. L. Braly, D. W. deQuilettes, L. M. Pazos-Outon, S. Burke, M. E. Ziffer, D. S. Ginger, H. W. Hillhouse, *Nat. Photonics* **2018**, *12*, 355.
[18] L. Krückemeier, B. Krogmeier, Z. Liu, U. Rau, T. Kirchartz, *Adv. Energy Mater.* **2021**, *11*, 2003489.
[19] A. Kiligaridis, P. A. Frantsuzov, A. Yangui, S. Seth, J. Li, Q. An, Y. Vaynzof, I. G. Scheblykin, *Nat. Commun.* **2021**, *12*, 3329.
[20] S. D. Stranks, V. M. Burlakov, T. Leijtens, J. M. Ball, A. Goriely, H. J. Snaith, *Phys. Rev. Appl.* **2014**, *2*, 034007.
[21] M. Taddei, S. Jariwala, R. J. E. Westbrook, S. Gallagher, A. C. Weaver, J. Pothoof, M. E. Ziffer, H. J. Snaith, D. S. Ginger, *ACS Energy Lett.* **2024**, *9*, 2508.
[22] P. W. Bridgman, *Phys. Rev.* **1928**, *31*, 101.
[23] P. Würfel, *Journal of Physics C-Solid State Physics* **1982**, *15*, 3967.
[24] W. Shockley, H. J. Queisser, *J. Appl. Phys* **1961**, *32*, 510.
[25] W. van Roosbroeck, W. Shockley, *Phys. Rev.* **1954**, *94*, 1558.
[26] C. L. Davies, M. R. Filip, J. B. Patel, T. W. Crothers, C. Verdi, A. D. Wright, R. L. Milot, F. Giustino, M. B. Johnston, L. M. Herz, *Nat. Commun.* **2018**, *9*, 293.
[27] Z. Liang, Y. Zhang, H. Xu, W. Chen, B. Liu, J. Zhang, H. Zhang, Z. Wang, D.-H. Kang, J. Zeng, X. Gao, Q. Wang, H. Hu, H. Zhou, X. Cai, X. Tian, P. Reiss, B. Xu, T. Kirchartz, Z. Xiao, S. Dai, N.-G. Park, J. Ye, X. Pan, *Nature* **2023**, *624*, 557.
[28] Y.-H. Lin, N. Sakai, P. Da, J. Wu, H. C. Sansom, A. J. Ramadan, S. Mahesh, J. Liu, R. D. J. Oliver, J. Lim, L. Aspitarte, K. Sharma, P. K. Madhu, A. B. Morales-Vilches, P. K. Nayak, S. Bai, F. Gao, C. R. M. Grovenor, M. B. Johnston, J. G. Labram, J. R. Durrant, J. M. Ball, B. Wenger, B. Stannowski, H. J. Snaith, *Science* **2020**, *369*, 96.
[29] D. Luo, W. Yang, Z. Wang, A. Sadhanala, Q. Hu, R. Su, R. Shivanna, G. F. Trindade, J. F. Watts, Z. Xu, T. Liu, K. Chen, F. Ye, P. Wu, L. Zhao, J. Wu, Y. Tu, Y. Zhang, X. Yang, W. Zhang, R. H. Friend, Q. Gong, H. J. Snaith, R. Zhu, *Science* **2018**, *360*, 1442.
[30] D. Luo, R. Su, W. Zhang, Q. Gong, R. Zhu, *Nat. Rev. Mater.* **2020**, *5*, 44.
[31] S. Teale, M. Degani, B. Chen, E. H. Sargent, G. Grancini, *Nat. Energy* **2024**, *9*, 779.
[32] H. Chen, C. Liu, J. Xu, A. Maxwell, W. Zhou, Y. Yang, Q. Zhou, A. S. R. Bati, H. Wan, Z. Wang, L. Zeng, J. Wang, P. Serles, Y. Liu, S. Teale, Y. Liu, M. I. Saidaminov, M. Li, N. Rolston, S. Hoogland, T. Filleter, M. G. Kanatzidis, B. Chen, Z. Ning, E. H. Sargent, *Science* **2024**, *384*, 189.
[33] Y. Shi, E. Rojas-Gatjens, J. Wang, J. Pothoof, R. Giridharagopal, K. Ho, F. Jiang, M. Taddei, Z. Yang, E. M. Sanehira, M. D. Irwin, C. Silva-Acuña, D. S. Ginger, *ACS Energy Lett.* **2022**, *7*, 4081.
[34] S. Jariwala, S. Burke, S. Dunfield, R. C. Shallcross, M. Taddei, J. Wang, G. E. Eperon, N. R. Armstrong, J. J. Berry, D. S. Ginger, *Chem. Mater.* **2021**, *33*, 5035.
[35] Q. Jiang, J. Tong, Y. Xian, R. A. Kerner, S. P. Dunfield, C. Xiao, R. A. Scheidt, D. Kuciauskas, X. Wang, M. P. Hautzinger, R. Tirawat, M. C. Beard, D. P. Fenning, J. J. Berry, B. W. Larson, Y. Yan, K. Zhu, *Nature* **2022**, *611*, 278.
[36] K. Suchan, T. J. Jacobsson, C. Rehermann, E. L. Unger, T. Kirchartz, C. M. Wolff, *Adv. Energy Mater.* **2024**, *14*, 2303420.
[37] Z. Liu, J. Siekmann, B. Klingebiel, U. Rau, T. Kirchartz, *Adv. Energy Mater.* **2021**, *11*, 2003386.
[38] J. E. Lee, S. G. Motti, R. D. J. Oliver, S. Yan, H. J. Snaith, M. B. Johnston, L. M. Herz, *Adv. Funct. Mater.* **2024**, *34*, 2401052.
[39] W. Xu, L. J. F. Hart, B. Moss, P. Caprioglio, T. J. Macdonald, F. Furlan, J. Panidi, R. D. J. Oliver, R. A. Pacalaj, M. Heeney, N. Gasparini, H. J. Snaith, P. R. F. Barnes, J. R. Durrant, *Adv. Energy Mater.* **2023**, *13*, 2301102.
[40] J. Hüpkes, U. Rau, T. Kirchartz, *Solar RRL* **2022**, *6*, 2100720.
[41] B. Das, Z. Liu, I. Aguilera, U. Rau, T. Kirchartz, *Mater. Adv.* **2021**, *2*, 3655.
[42] O. Almora, G. C. Bazan, C. I. Cabrera, L. A. Castriotta, S. Erten-Ela, K. Forberich, K. Fukuda, F. Guo, J. Hauch, A. W. Y. Ho-Baillie, T. J. Jacobsson, R. A. J. Janssen, T. Kirchartz, R. R. Lunt, X. Mathew, D. B. Mitzi, M. K. Nazeeruddin, J. Nelson, A. F. Nogueira, U. W. Paetzold, B. P. Rand, U. Rau, T. Someya, C. Sprau, L. Vaillant-Roca, C. J. Brabec, *Adv. Energy Mater.* **2025**, *15*, 2404386.
[43] T. Kirchartz, G. Yan, Y. Yuan, B. K. Patel, D. Cahen, P. K. Nayak, *Nat. Rev. Mater.* **2025**, *10*, 335.
[44] N. P. Jasti, I. Levine, Y. Feldman, G. Hodes, S. Aharon, D. Cahen, *Proc. Natl. Acad. Sci. USA* **2024**, *121*, 2316867121.
[45] D. Cahen, L. Kronik, G. Hodes, *ACS Energy Lett.* **2021**, *6*, 4108.
[46] Y. Yan, W. J. Yin, T. Shi, W. Meng, C. Feng, *Defect Physics of $CH_3NH_3PbX_3$(X = I, Br, Cl) Perovskites*, Springer International Publishing, Berlin **2016**, p. 79.
[47] W. J. Yin, T. Shi, Y. Yan, *Appl. Phys. Lett.* **2014**, *104*, 063903.
[48] I. Mosquera-Lois, Y.-T. Huang, H. Lohan, J. Ye, A. Walsh, R. L. Z. Hoye, *Nat. Rev. Chem.* **2025**, *9*, 287.
[49] S. Feldmann, S. Macpherson, S. P. Senanayak, M. Abdi-Jalebi, J. P. H. Rivett, G. Nan, G. D. Tainter, T. A. S. Doherty, K. Frohna, E. Ringe, R. H. Friend, H. Sirringhaus, M. Saliba, D. Beljonne, S. D. Stranks, F. Deschler, *Nat. Photonics* **2020**, *14*, 123.
[50] Y. Yuan, G. Yan, C. Dreessen, T. Kirchartz, *Adv. Energy Mater.* **2025**, *15*, 2403279.
[51] Y. Yuan, G. Yan, S. Akel, U. Rau, T. Kirchartz, *Sci. Adv.* **2025**, *11*, adt1171.
[52] Y. Yuan, G. Yan, C. Dreessen, T. Rudolph, M. Hülsbeck, B. Klingebiel, J. Ye, U. Rau, T. Kirchartz, *Nat. Mater.* **2024**, *23*, 391.
[53] W. Shockley, W. T. Read, *Phys. Rev.* **1952**, *87*, 835.
[54] R. N. Hall, *Phys. Rev.* **1952**, *87*, 387.
[55] T. Markvart, *Multiphonon Recombination*, Cambridge University Press, Cambridge **2003**, p. 470.
[56] T. Markvart, *J. Phys. C: Solid State Phys.* **1981**, *14*, L895.
[57] J. Benduhn, K. Tvingstedt, F. Piersimoni, S. Ullbrich, Y. Fan, M. Tropiano, K. A. McGarry, O. Zeika, M. K. Riede, C. J. Douglas, S. Barlow, S. R. Marder, D. Neher, D. Spoltore, K. Vandewal, *Nat. Energy* **2017**, *2*, 17053.
[58] R. A. Marcus, *J. Electroanal. Chem.* **2000**, *483*, 2.
[59] U. Rau, *Phys. Rev. B* **2007**, *76*, 085303.
[60] R. T. Ross, *J. Chem. Phys.* **1967**, *46*, 4590.
[61] B. Das, I. Aguilera, U. Rau, T. Kirchartz, *Phys. Rev. Mater.* **2020**, *4*, 024602.
[62] D. A. Egger, A. Bera, D. Cahen, G. Hodes, T. Kirchartz, L. Kronik, R. Lovrincic, A. M. Rappe, D. R. Reichman, O. Yaffe, *Adv. Mater.* **2018**, *30*, 1800691.
[63] O. Yaffe, Y. Guo, L. Z. Tan, D. A. Egger, T. Hull, C. C. Stoumpos, F. Zheng, T. F. Heinz, L. Kronik, M. G. Kanatzidis, J. S. Owen, A. M. Rappe, M. A. Pimenta, L. E. Brus, *Phys. Rev. Lett.* **2017**, *118*, 136001.
[64] T. Markvart, *Multiphonon Recombination*, Cambridge University Press, Cambridge **2003**, p. 475.
[65] L. D. Whalley, P. van Gerwen, J. M. Frost, S. Kim, S. N. Hood, A. Walsh, *J. Am. Chem. Soc.* **2021**, *143*, 9123.
[66] T. Markvart, *Multiphonon Recombination*, Cambridge University Press, Cambridge **2003**, p. 467.
[67] B. K. Ridley, *Solid-State Electron.* **1978**, *21*, 1319.
[68] B. K. Ridley, *J. Phys. C: Solid State Phys.* **1978**, *11*, 2323.
[69] J. M. Richter, M. Abdi-Jalebi, A. Sadhanala, M. Tabachnyk, J. P. H. Rivett, L. M. Pazos-Outon, K. C. Gödel, M. Price, F. Deschler, R. H. Friend, *Nat. Commun.* **2016**, *7*, 13941.

[70] F. Staub, I. Anusca, D. C. Lupascu, U. Rau, T. Kirchartz, *J. Phys.: Mater.* **2020**, *3*, 025003.
[71] M. H. Du, *J. Phys. Chem. Lett.* **2015**, *6*, 1461.
[72] X. Zhang, M. E. Turiansky, J.-X. Shen, C. G. Van de Walle, *Phys. Rev. B* **2020**, *101*, 140101.
[73] D. Meggiolaro, S. G. Motti, E. Mosconi, A. J. Barker, J. Ball, C. Andrea Riccardo Perini, F. Deschler, A. Petrozza, F. De Angelis, *Energy Environ. Sci.* **2018**, *11*, 702.
[74] D. Meggiolaro, F. De Angelis, *ACS Energy Lett.* **2018**, *3*, 2206.
[75] S. G. Motti, D. Meggiolaro, S. Martani, R. Sorrentino, A. J. Barker, F. De Angelis, A. Petrozza, *Adv. Mater.* **2019**, *31*, 1901183.
[76] J. Zhang, X. Zhang, M. E. Turiansky, C. G. Van de Walle, *PRX Energy* **2023**, *2*, 013008.
[77] J. Heyd, G. E. Scuseria, M. Ernzerhof, *J. Chem. Phys.* **2003**, *118*, 8207.
[78] F. Peña-Camargo, J. Thiesbrummel, H. Hempel, A. Musiienko, V. M. L. Corre, J. Diekmann, J. Warby, T. Unold, F. Lang, D. Neher, M. Stolterfoht, *Appl. Phys. Rev.* **2022**, *9*, 021409.
[79] S. Rein, T. Rehrl, W. Warta, S. W. Glunz, *J. Appl. Phys.* **2002**, *91*, 2059.
[80] A. Richter, S. W. Glunz, F. Werner, J. Schmidt, A. Cuevas, *Phys. Rev. B* **2012**, *86*, 165202.
[81] R. A. Sinton, A. Cuevas, *Appl. Phys. Lett.* **1996**, *69*, 2510.
[82] J. Siekmann, A. Kulkarni, S. Akel, B. Klingebiel, M. Saliba, U. Rau, T. Kirchartz, *Adv. Energy Mater.* **2023**, *13*, 2300448.
[83] O. Gunawan, S. R. Pae, D. M. Bishop, Y. Virgus, J. H. Noh, N. J. Jeon, Y. S. Lee, X. Shao, T. Todorov, D. B. Mitzi, B. Shin, *Nature* **2019**, *575*, 151.
[84] B. Grimm, V. Steckenreiter, A. Raugewitz, F. Haase, R. Brendel, R. Peibst, J. Schmidt, *Phys. Status Sol. (RRL)* **2025**, *19*, 2400386.
[85] Y. Li, Z. Jia, Y. Yang, F. Yao, Y. Liu, Q. Lin, *Appl. Phys. Rev.* **2023**, *10*, 011406.
[86] X. Zhu, W. Xiong, C. Hu, K. Mo, M. Yang, Y. Li, R. Li, C. Shen, Y. Liu, X. Liu, S. Wang, Q. Lin, S. Yuan, Z. Liu, Z. Wang, *Adv. Mater.* **2024**, *36*, 2309487.
[87] U. Rau, U. W. Paetzold, T. Kirchartz, *Phys. Rev. B* **2014**, *90*, 035211.
[88] F. Staub, T. Kirchartz, K. Bittkau, U. Rau, *J. Phys. Chem. Lett.* **2017**, *8*, 5084.
[89] P. Asbeck, *J. Appl. Phys.* **1977**, *48*, 820.
[90] L. Krückemeier, Z. Liu, B. Krogmeier, U. Rau, T. Kirchartz, *Adv. Energy Mater.* **2021**, *11*, 2102290.
[91] T. Kirchartz, *Chem. Sci.* **2025**, *16*, 8153.
[92] E. Gutierrez-Partida, M. Rusu, F. Zu, M. Raoufi, J. Diekmann, N. Tokmoldin, J. Warby, D. Menzel, F. Lang, S. Shah, S. Shoaee, L. Korte, T. Unold, N. Koch, T. Kirchartz, D. Neher, M. Stolterfoht, *ACS Appl. Mater. Interfaces* **2025**, *17*, 11176.
[93] B. Das, I. Aguilera, U. Rau, T. Kirchartz, *Adv. Opt. Mater.* **2022**, *10*, 2101947.
[94] T. Leijtens, S. D. Stranks, G. E. Eperon, R. Lindblad, E. M. J. Johansson, I. J. McPherson, H. Rensmo, J. M. Ball, M. M. Lee, H. J. Snaith, *ACS Nano* **2014**, *8*, 7147.
[95] A. Marunchenko, J. Kumar, A. Kiligaridis, S. M. Rao, D. Tatarinov, I. Matchenya, E. Sapozhnikova, R. Ji, O. Telschow, J. Brunner, A. Yulin, A. Pushkarev, Y. Vaynzof, I. G. Scheblykin, *J. Phys. Chem. Lett.* **2024**, *15*, 6256.
[96] A. Marunchenko, J. Kumar, A. Kiligaridis, D. Tatarinov, A. Pushkarev, Y. Vaynzof, I. G. Scheblykin, *ACS Energy Lett.* **2024**, *9*, 2075.
[97] T. Kirchartz, J. Bisquert, I. Mora-Sero, G. Garcia-Belmonte, *Phys. Chem. Chem. Phys.* **2015**, *17*, 4007.
[98] A. Maurano, R. Hamilton, C. G. Shuttle, A. M. Ballantyne, J. Nelson, B. O'Regan, W. M. Zhang, I. McCulloch, H. Azimi, M. Morana, C. J. Brabec, J. R. Durrant, *Adv. Mater.* **2010**, *22*, 4987.
[99] C. G. Shuttle, A. Maurano, R. Hamilton, B. O'Regan, J. C. de Mello, J. R. Durrant, *Appl. Phys. Lett.* **2008**, *93*, 183501.
[100] F. Deledalle, P. S. Tuladhar, J. Nelson, J. R. Durrant, T. Kirchartz, *J. Phys. Chem. C* **2014**, *118*, 8837.
[101] D. Rauh, C. Deibel, V. Dyakonov, *Adv. Funct. Mater.* **2012**, *22*, 3371.
[102] Z. Liu, L. Krückemeier, B. Krogmeier, B. Klingebiel, J. A. Marquez, S. Levcenko, S. Öz, S. Mathur, U. Rau, T. Unold, T. Kirchartz, *ACS Energy Lett.* **2019**, *4*, 110.
[103] R. E. Brandt, V. Stevanoviç, D. S. Ginley, T. Buonassisi, *MRS Commun.* **2015**, *5*, 265.
[104] C.-T. Sah, W. Shockley, *Phys. Rev.* **1958**, *109*, 1103.
[105] A. Musiienko, F. Yang, T. W. Gries, C. Frasca, D. Friedrich, A. Al-Ashouri, E. Sağlamkaya, F. Lang, D. Kojda, Y.-T. Huang, V. Stacchini, R. L. Z. Hoye, M. Ahmadi, A. Kanak, A. Abate, *Nat. Commun.* **2024**, *15*, 316.
[106] S. M. Rao, A. Kiligaridis, A. Yangui, Q. An, Y. Vaynzof, I. G. Scheblykin, *Adv. Opt. Mater.* **2024**, *12*, 2300996.
[107] R. E. Brandt, R. C. Kurchin, V. Steinmann, D. Kitchaev, C. Roat, S. Levcenco, G. Ceder, T. Unold, T. Buonassisi, *Joule* **2017**, *1*, 843.
[108] M. Kober-Czerny, A. Dasgupta, S. Seo, F. M. Rombach, D. P. McMeekin, H. Jin, H. J. Snaith, *PRX Energy* **2025**, *4*, 013001.
[109] C. Kupfer, V. M. Le Corre, C. Li, L. Lüer, K. Forberich, M. Kato, A. Osvet, C. J. Brabec, *J. Mater. Chem. C* **2024**, *12*, 95.
[110] T. Kirchartz, B. Das, *J. Phys.: Energy* **2023**, *5*, 031001.
[111] H. Zhan, V. Ahmad, A. Mayon, G. Dansoa Tabi, A. D. Bui, Z. Li, D. Walter, H. Nguyen, K. Weber, T. White, K. Catchpole, *Energy Environ. Sci.* **2024**, *17*, 4735.
[112] J. Xu, A. Maxwell, M. Wei, Z. Wang, B. Chen, T. Zhu, E. H. Sargent, *ACS Energy Lett.* **2021**, *6*, 4220.

**Jürgen Hüpkes** is a senior researcher at the Research Centre Jülich (IMD-3 Photovoltaics, Surface Physics group). He received his doctoral degree in physics at the RWTH Aachen University, Germany. His research first focused on the development of transparent conductive materials for solar cells. In recent years, he has been analyzing recombination mechanisms in perovskite solar cells using modeling and surface physical methods.

**Uwe Rau** was the Director of the IMD-3 Photovoltaics at Research Centre Jülich until 2/2025. He is Professor (em.) at RWTH Aachen, Faculty of Electrical Engineering and Information Technology. Previously, he was a senior researcher at the University Stuttgart as well as a postdoc at the University Bayreuth and at the Max-Planck-Institute for Solid State Research in Stuttgart. His research interest covers electronic and optical properties of semiconductors and semiconductor devices, especially characterization, simulation, and technology of solar cells and solar modules.

**Thomas Kirchartz** is currently a professor of electrical engineering and information technology at the University Duisburg-Essen, the deputy director of the IMD-3 Photovoltaics, the head of the department of Knowledge-based photovoltaics and the group of Optical Spectroscopy at the Research Centre Jülich (Institute for Energy and Climate Research). Previously, he was a Junior Research Fellow at Imperial College London. His research interests include all aspects of the fundamental understanding of photovoltaic devices, including their characterization and simulation.